# THE UV SPECTROSCOPY OF 3-PHENYL-2-PROPYNENITRILE AND ITS METHYLATED DERIVATIVES

by

**Khadija M. Jawad**

**A Dissertation**

*Submitted to the Faculty of Purdue University*

*In Partial Fulfillment of the Requirements for the degree of*

**Doctor of Philosophy**


Department of Chemistry

West Lafayette, Indiana

May 2019

# THE PURDUE UNIVERSITY GRADUATE SCHOOL
# STATEMENT OF COMMITTEE APPROVAL

Dr. Timothy Zwier, Chair
Department of Chemistry
Dr. Lyudmila Slipchenko
Department of Chemistry
Dr. Paul Wenthold
Department of Chemistry
Dr. Dor Ben-Amotz
Department of Chemistry

**Approved by:**
Dr. Christine Hrycyna
Head of the Graduate Program

*For my parents, Mouin and Brenda Jawad.*

*I will always love you.*

# ACKNOWLEDGMENTS

First and foremost, I want to thank Deepali Mehta-Hurt for all her patience, encouragement, and guidance as I made my way through graduate school: if I deserve this degree, it's only because of you.

The Chemistry Department is full of wonderful people who deserve to be thanked as well: I've had the privilege to work with people from Zones, Chem Shop, Chem Stores, JAFCI, Business Office, Procurement, the Main Office, Copy Center, General Chemistry. Several of them deserve special mention: Tim Selby who was always a great help when lasers broke down; Dr. Ryan Hilger, who basically built a special pulse valve for us using a piezoelectric stack as the driving force; Ned Gangwer and Betty Dexter who have been wonderful friends and always a joy to interact with and a great help when things went wrong in the lab; Betty Hatfield, Debbie Packer, Lynn Rider, Darci DeCamp, Suzy Gustafson, and Trisha Herrera for not only doing their jobs well and always accommodating us graduate students, but for also helping me with my baby boy as I tried getting this thesis done these last months, and never having a problem with me when I brought him in (thank you all so much for your help!); and Rob Reason, for being you and being great.

Those who've been helpful as I tried working on my projects include all my collaborators: Claudia Viquez-Rojas, without whom we'd have no clue how to explain things, and her advisor Dr. Lyudmila Slipchenko; Dr. Anthony Tomaine and Joey Bungard for synthesizing the methylated PPNs for me; Sean Fritz for the microwave work; Josh Fischer for helping me double check some of the methyl PPN LIF data; and Drs. Joe Korn, Patrick Walsh, Joe Gord, and Dan Hewett for teaching me the instrumentation and science.

Finally, I want to thank my family, especially my sisters Aliya Jawad and Sara Saleh, for always being supportive and loving even when their lives are busy and complicated. To my

husband, John Lawler, I love you so much, you've been my support, never once let me give up on the science and spend the rest of my life baking (still not a bad way to spend my life, I think!), and you've been so patient these past few months. My baby boy, John (Yehya) Lute Lawler, deserves a mention too, he's made my life so much rosier than it was, his smiles, his laughter, and his hugs make my days complete, and I love you!

# TABLE OF CONTENTS

# LIST OF TABLES

# LIST OF FIGURES

# ABSTRACT

Author: Jawad, Khadija, M. PhD
Institution: Purdue University
Degree Received: May 2019
Title: The UV Spectroscopy of 3-Phenyl-2-Propynenitrile and its Methylated Derivatives
Committee Chair: Timothy Zwier

For decades there has been interest in understanding early prebiotic Earth, including its atmospheric chemistry. Saturn's moon Titan is the only other body in our Solar System with an atmosphere thought to resemble that of early Earth's, and for this reason it has garnered a lot of attention over the years. Much is now known about the smaller molecules present in that atmosphere, starting with the most abundant, $N_2$ and $CH_4$, and going up to slightly larger molecules such as cyanoacetylene and benzene. As the molecules get larger, however, so does the gap in knowledge, especially as it pertains to nitriles. This dissertation aims to add to the story of Titan's nitriles by first characterizing a molecule thought to be the photochemical product of the reaction between cyanoacetylene and benzene, 3-phenyl-2-propyne-nitrile (PPN). The UV spectra of PPN proved immensely interesting due to the strong presence of in-plane and out-of-plane vibrations of $b_2$ and $b_1$ symmetry, respectively. This is possibly a result of strong vibronic coupling between several excited electronic states or Coriolis coupling between complementary $b_1$ and $b_2$ vibrational levels. The multi-layer extension of the multi-configuration time dependent Hartree (ML-MCTDH) algorithm was used to understand how the excited states and the vibrational levels might interact, and emission and absorption spectra were modeled and compared to the experimental spectra. The second group of molecules studied included the *ortho*-, *meta*-, and *para*-methyl PPN. Strong methyl rotor activity is seen in the *m*-methyl PPN, with some activity in the *p*-methyl PPN. The methyl rotor activity in the *m*-methyl PPN is similar to other *meta*-substituted toluenes, and allows

us to describe the methyl rotor barrier height in both ground and excited electronic state. Additionally, in all three methylated PPNs we see evidence for strong vibronic coupling in the abundance of out-of-plane vibrations, as had been seen in PPN.

# CHAPTER 1. INTRODUCTION

## 1.1 Background

Saturn's Titan is the largest moon in our solar system and the only other body with an atmosphere similar to Earth's in that it is dominated by nitrogen gas. However, unlike the Earth of today, the next dominant chemical species is methane at 1-3%,[1] making Titan's atmosphere resemble the reducing atmosphere thought to be present in prebiotic Earth.[2, 4] Additionally, while Earth has a water cycle, Titan has a methanological cycle: lakes and rivers of methane and other organics exist on the surface, while clouds of methane race across the sky.[1-3] For these reasons Titan poses as a good source of information – and even as a test subject – for scientists trying to understand the chemical processes active in prebiotic Earth.

Titan's atmosphere has a dense orange haze, and scientists have spent decades trying to identify the molecules responsible for this haze. Not surprisingly, nitrogen-containing molecules are thought to be important in describing both Titan's and early Earth's atmospheric chemistry. The chemistry that can take place in Titan's atmosphere involves both neutral and ion reactions: energy available as sunlight or energetic particles from Saturn's magnetosphere breaks bonds or ionizes the $N_2$ and $CH_4$ in Titan's atmosphere, leading them to react with each other.[1] The smallest products of these reactions include $C_2H_6$, $C_2H_4$, $C_4H_2$, as well as the nitrogen-containing organic molecules HCN, $HC_3N$, and $C_2N_2$.[1] From that point, more photochemistry utilizing longer wavelengths not absorbed by the $N_2$ or $CH_4$ can take place between the larger molecules, thus building up the library of chemicals in Titan's atmosphere to include complex organic, aromatic, and heteroaromatic species, with the nitrile moiety of particular interest to us because of its increased stability relative to other functionals.[5]

Over the past several years, the Zwier group has carried out laboratory studies of the UV spectroscopy and photochemistry of Titan's atmosphere that push the models of the atmosphere at their large-molecule limit.[6] To date, the major source of observational spectroscopic and spectrometric data on Titan's atmosphere comes from NASA's Cassini spacecraft, which made several passes of Titan, and the Huygens probe, which was sent down to Titan's surface.[7] However, knowledge of what molecules are responsible for specific features in the spectra is still lacking, either because the UV and IR absorption are not known or have not been studied at the low temperatures relevant to Titan. This necessitates the generation of atmospheric models and motivates laboratory studies[6, 14-16] to identify likely species, estimating their abundances, and studying their photochemistry. The atmospheric models act as a guide for experimentalists in that they suggest likely reactions using known reactants, although, lacking experimental data, they often simplify the products at the large-molecule end of their models into one category: "polymer."[8-16] Our research group's work has historically been able to obtain and analyze the UV spectrum of possible molecules in this larger size range, including many benzene derivatives. We have occasionally also conducted studies of photochemical reactions between known species to identify specific products.[17-18] Such studies can be matched up to spectra taken by Cassini-Huygens, which in turn adds to the atmospheric models by confirming which chemical species are present and how they may photochemically react on Titan. The comparison between our UV spectra and the observations made by Cassini-Huygens is appropriate in that the temperature of Titan's atmosphere is approximately 80K, while our experiments are able to vibrationally cool the molecules down to 10K at the lowest extreme.

## 1.2 Organization of Thesis

The aim of this thesis is to describe the spectroscopy of four related nitrile-containing molecules that are relevant to Titan's atmosphere: 3-phenyl-2-propynenitrile and its methyl derivatives 3-(2-methylphenyl)-2-propynenitrile, 3-(3-methylphenyl)-2-propynenitrile, and 3-(4-methylphenyl)-2-propynenitrile, which will be abbreviated as PPN, *o*-methyl PPN, *m*-methyl PPN, and *p*-methyl PPN, respectively.

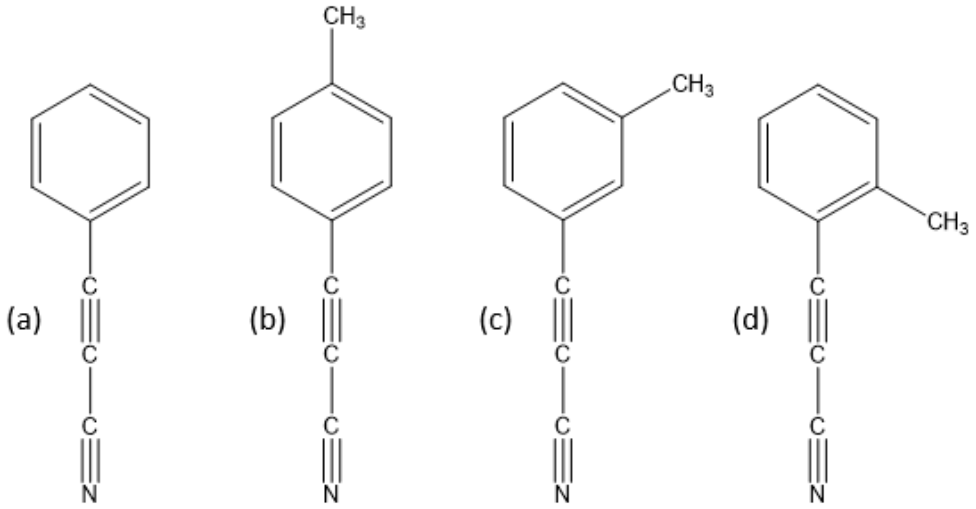


Figure 1.1 (a) PPN, (b) *p*-methyl PPN, (c) *m*-methyl PPN, and (d) *o*-methyl PPN.

All four molecules could be the result of the photochemical reactions between cyanoacetylene ($HC_3N$) and either benzene (in the case of PPN)[17] or toluene (in the cases of all three methylated PPN species). The UV spectra of PPN, described in Chapter 3, showed some interesting and unexpected features that called into question the excited states being accessed and the geometry of those excited states. Previous work has been done on a similar reaction between diacetylene and benzene, producing the hydrocarbon analog of PPN, phenyldiacetylene.[18]

However, the analog's UV spectrum yielded only broad peaks attributed to the C≡C bond stretch, and was thus of very little help in understanding the PPN spectra. Furthermore, PPN's excited state lifetime contained two components, a short-lived and a long-lived part, that suggested similarities to diphenyldiacetylene[19] and phenylacetylene and benzonitrile.[19-24] For that reason, the methylated versions of PPN were studied (Chapter 4), as the methyl rotor is sensitive to the electronic environment of the ring and, therefor, can help describe the excited state.

## 1.3 References


1. Raulin, F., et. al., Chem. Soc. Rev., 2012. **41** (16): p. 5380-5393.
2. Balucani, N., Chem. Soc. Rev., 2012. **41** (16): p. 5473-5483.
3. Tobie, G., D. Gautier, and F. Hersant, The Astrophysical Journal, 2012. **752** (2): p. 125.
4. Kasting, J.F., Science, 1993. **259**: p. 920-926.
5. Bernstein, M.P., et. al., The Astrophysical Journal, 2004. **601** (1): p. 365.
6. Cable, M.L., et. al., Chem. Rev., 2012. **112** (3): p. 1882-1909.
7. Waite, J.H., et. al., Science, 2007. **316** (5826): p. 870-875.
8. Krasnopolsky, V.A., Icarus, 2009. **201** (1): p. 226-256.
9. Yung, Y.L., Icarus, 1987. **72**: p. 468-472.
10. Wilson, E.H. and S.K. Atreya, Journal of Geophysical Research-Planets, 2004. **109** (E6).
11. Krasnopolsky, V.A., Planetary and Space Science, 2010. **58** (12): p. 1507-1515.
12. Banaszkiewicz, M., et. al., Icarus, 2000. **147** (2): p. 386-404.
13. Krasnopolsky, V.A., Icarus, 2014. **236** (0): p. 83-91.
14. Tran, B.N., et. al., Icarus, 2005. **177**: p. 106-115.
15. Ferris, J., et. al., Adv. in Space Research, 2005. **36**: p. 251-257.
16. Ali. A., et. al., Planetary and Space Science, 2015. **109**: p. 46-63.
17. Krasnopolsky, V.A., Icarus, 2009. **201**: p. 226-256.

18. Robinson, A.G., et. al., J. Phys. Chem. A, 2000. **104**: p. 10312-10320.

19. Sebree, J.A. and T.S. Zwier, Phys. Chem. Chem. Phys., 2012. **14**: p. 173-183.

20. Hofstein, J., et. al., J. Phys. Chem. A, 2008. **112**: p. 1195-1201.

21. Johnson, P.M. and T.J. Sears, J. Chem. Phys., 2015. **143**: 044305.

22. Johnson, P.M. and T.J. Sears, J. Phys. Chem. A, 2013. **117**: p. 7786-7793.

23. Helm, R.M., et. al., Chem. Phys. Let., 1997. **270**: p. 285-292.

24. Ribblett, J.W., et. al., J. Chem. Phys., 1999. 111: p. 8454-8461.

# CHAPTER 2. EXPERIMENTAL

This chapter describes in detail the various instruments and techniques used throughout the projects presented in this dissertation.

## 2.1 Supersonic Expansion:

Regardless of the instrument used to obtain our data, the molecules are always cooled into their zero-point vibrational state prior to interrogation. This is accomplished via a process called supersonic expansion: the liquid or solid analyte is placed on cotton or glass wool and inserted into the sample holder compartment of either a Series 9 general valve (fluorescence and microwave chambers, sections 2.2.2. and 2.2.3. respectively) or a Jordan valve (time-of-flight mass spectrometer chamber, section 2.2.1.). Should the analyte have a low vapor pressure, the valves are heated to an appropriate temperature to sufficiently increase the number of molecules in the gas phase to see signal. The general valve is heated using a heating rope whose current is regulated with a Variac, while the Jordan valve is warmed with a heating cartridge embedded within it, also controlled with a Variac. A nonreactive buffer gas - most commonly a noble gas such as helium or argon – is used to carry the gaseous analyte into the vacuum chamber by way of a 500 μm diameter orifice. The resulting expansion out into the chamber involves many collisions between the analyte and the buffer gas, and with each collision energy is transferred away from the analyte. Eventually, all the analyte molecules are left with little or no vibrational energy, and any spectroscopic data is thereby simplified to discrete, rather than broad, peaks.

## 2.2 Vacuum Chambers

### 2.2.1 Time-of-flight mass spectrometer chamber

Figure 2.1 represents the time-of-flight mass spectrometer vacuum chamber used in this work. This chamber is unusual in that it has no skimmer to separate source and ionization regions. This geometry has been designed to make for open access to the molecules for laser excitation during photochemical studies – which were not conducted for this thesis. Instead, the chamber was used to record ultraviolet spectra of the molecules of interest using resonant two-photon ionization (for further information see section 2.4.2). The analyte molecules in the supersonic expansion expand freely into the ion source region, whose center is about 8 cm from the front face of the Jordan valve. The molecules are intersected there by the frequency-doubled light from a dye laser or an optical parametric oscillator (OPO) pumped by a Nd:YAG laser. If the UV light is resonant with a transition of the analyte molecule, a fraction of the molecules will be excited to a higher electronic state. Then, if the ionization potential is low enough, another photon of the same frequency will be sufficient to ionize the molecule – this is called one-color resonant two photon ionization (1C-R2PI). When the ionization potential is too large to use the same wavelength of light for both excitation and ionization steps, then another laser at a higher frequency is used to ionize the molecules. This is called two-color R2PI (2C-R2PI). Once ionized, the molecules are directed down the path of the time-of-flight (a Wiley-McLaren TOF) component of the chamber until they are detected by the microchannel plate (MCP). In this way, only species that are resonant with the laser can be detected. Additionally, any impurities that might get ionized due to multi-photon processes and are detected by the MCP can be ignored as this technique is mass-resolved.

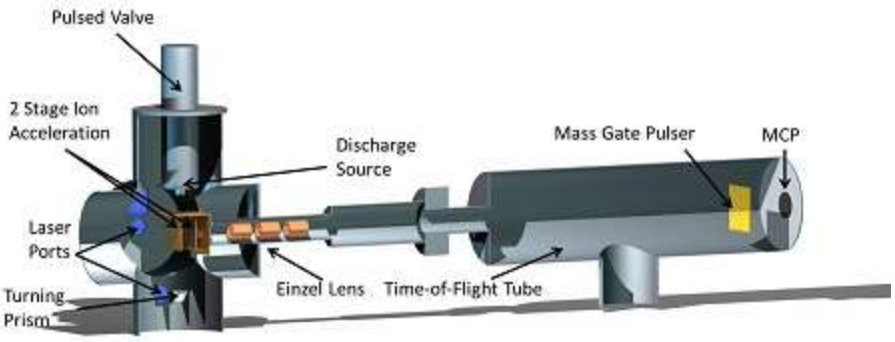


Figure 2.1 Schematic of the time-of-flight mass spectrometry instrument

### 2.2.2 Fluorescence chamber

Laser-induced fluorescence (LIF) provides an alternative to R2PI that gives up mass resolution but produces additional information not available in R2PI measurements. Figure 2.2 represents a schematic of the LIF instrument. As in the R2PI chamber, the molecules undergo a free jet expansion into the vacuum chamber, where they are interrogated typically about 1 cm downstream from the nozzle orifice. The molecules are excited with a single photon to an excited electronic state, and their resulting fluorescence is collected by two mirrors, and directed perpendicular to and away from the laser light to minimize scatter. The light is then focused, turned perpendicular again by a UV-reflective mirror, and passed through one or more long-pass filters to reduce the scattered laser light before striking a UV-sensitive photomultiplier tube (PMT). LIF excitation scans are recorded by collecting the total fluorescence as a function of excitation laser wavelength.

Alternatively, once a vibrationally-resolved electronic transition (‘vibronic’) has been detected, the excitation laser wavelength can be fixed on that transition, and the emission dispersed through a monochromator to obtain a dispersed fluorescence (DF) spectrum. To accomplish this, the last mirror is moved out of the beam path, allowing the light to hit another mirror and be

focused by a second lens onto the entrance slit of a HORIBA Jobin Yvon .75 meter monochromator. A gated, Andor intensified charge-coupled device (iCCD) is placed at the exit plane of the monochromator and collects the dispersed light.

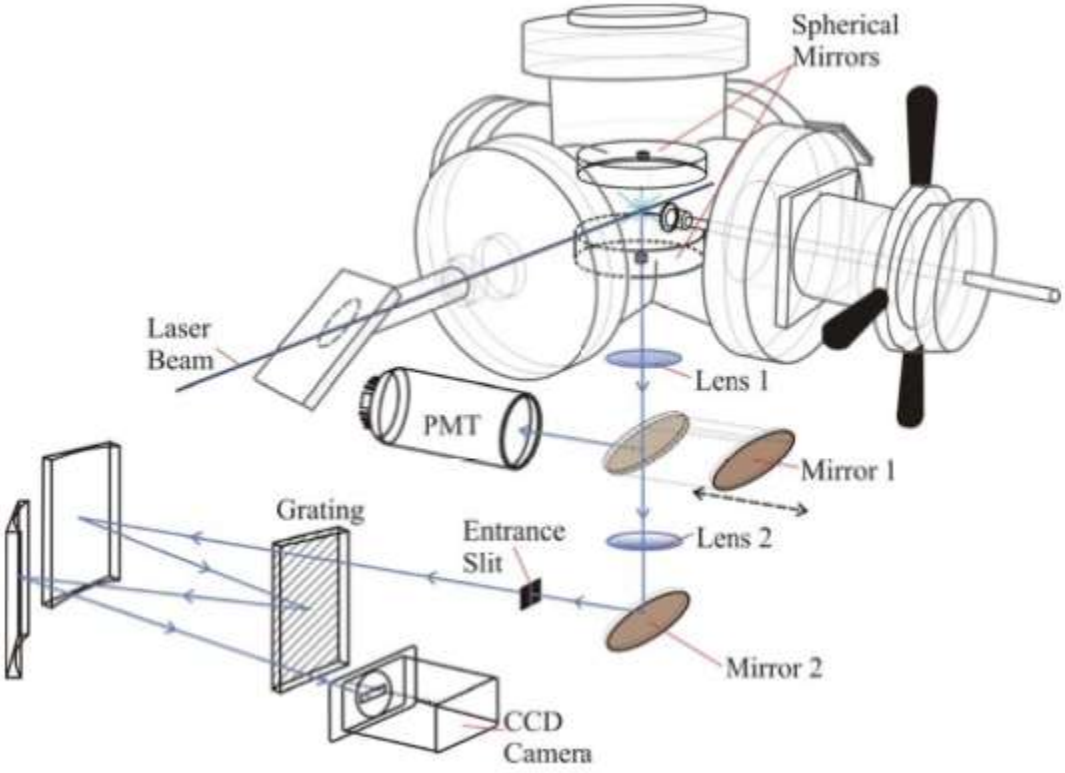


Figure 2.2 Schematic of the laser-induced fluorescence chamber

### 2.2.3 Broadband chirped pulse Fourier transform microwave spectrometer

The rotational spectrum was recorded in the 8–18 GHz region using a broadband chirped pulse Fourier transform microwave (CP-FTMW) spectrometer (Fig. 2.3).

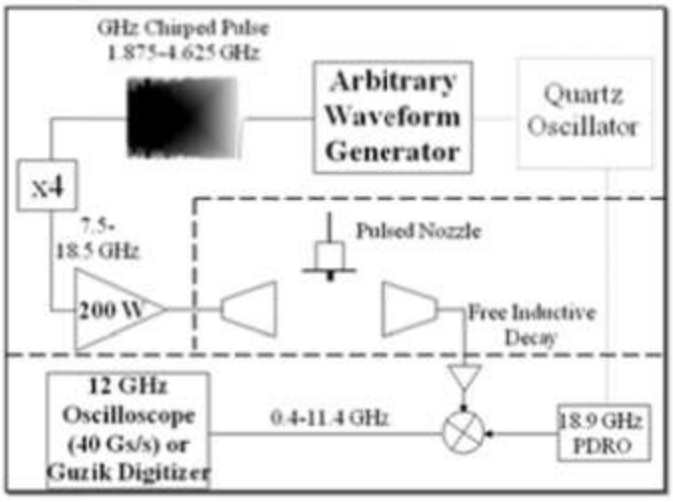


Figure 2.3 Simplified schematic of the CP-FTMW instrument

A 10 GS/s arbitrary waveform generator (AWG; Tektronix AWG7101) is used to generate the broadband chirps that are then amplified by a 200 W travelling wave tube amplifier (TWTA; Amplifier Research 200T8G18A). The microwave pulses are introduced into the vacuum chamber via a broadcasting horn, where they interact with the molecules in the supersonic expansion, polarizing them. The resulting free induction decay (FID) is collected by a collection horn. The molecular emission is amplified with a low noise amplifier (Miteq AMF-6F06001800-15-10P), down-converted by mixing with a phase locked dielectric resonator oscillator (PLDRO, Microwave Dynamics PLO-2000-18.90) at 18.9 GHz and phase coherently averaged and digitized over a 16 μsec time window by a 13 GHz, 40 GS/s real-time digitizer (Guzik ADC6131). The time-domain signal is then filtered with a Kaiser-Bessel function and Fast Fourier Transformed using a custom MATLAB routine to obtain the final frequency domain spectrum. The process to fit the spectrum is described in Chapter 3.3.5.

## 2.3 Computational Methods

To aid in understanding the experimental spectra we run a variety of computational calculations which provide us with the optimized geometries, energies, and harmonic vibrational frequencies of each particular electronic state. The calculations also provide us with oscillator strengths and excitation energies required to go from one state to another. The specific methods employed for each project will be discussed in the following chapters.

## 2.4 Spectroscopy Methods

### 2.4.1 Fluorescence methods

The simplest method to obtain the excitation spectra of a fluorescent species is by the one-laser technique of LIF (Fig. 2.4) whereby the frequency doubled ultraviolet (UV) output of a dye laser can be aligned and timed to intersect the cooled analyte in the supersonic expansion. The laser is tuned through the wavelength region of interest, and, when the laser is resonant with a transition in the molecule, absorption is followed by fluorescence. The total fluorescence is collected and directed towards a photomultiplier tube (PMT), and the spectrum is generated by plotting fluorescence against excitation wavelength.

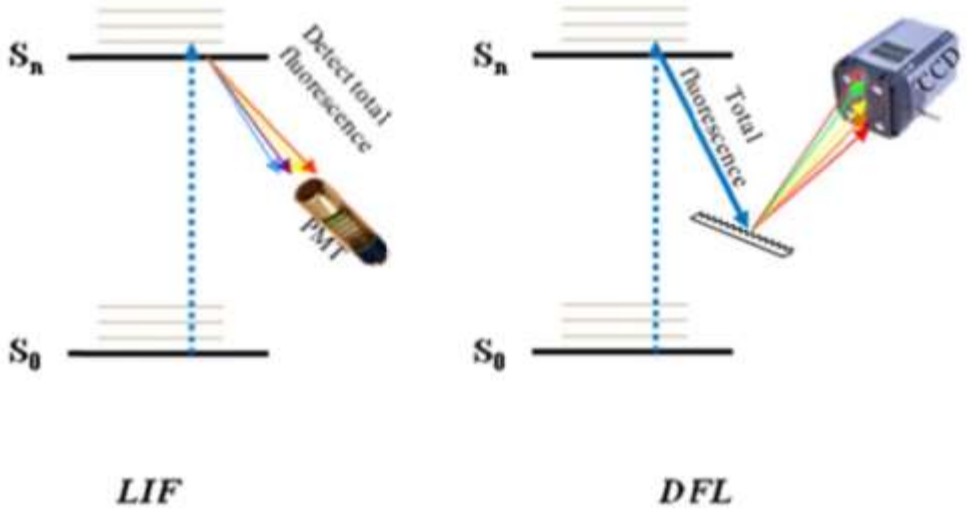


Figure 2.4 Schemes for LIF and DFL

Dispersed fluorescence (DFL) is used to obtain ground state spectra by pumping a specific transition in the excitation spectrum and directing the total fluorescence into a monochromator, where it is dispersed into its constituent wavelengths and collected on an iCCD.

### 2.4.2 Resonant two-photon ionization

In cases where the fluorescence quantum yield is low or where impurities in the sample interfere with fluorescence signal, resonant two-photon ionization (R2PI) becomes a powerful mass-resolved tool of choice. In a one-color R2PI experiment (1C-R2PI), the frequency doubled UV output of a dye laser or a tunable solid-state laser is aligned and timed to intersect the analyte as before. The laser is tuned over the wavelength region of interest, and when the laser is resonant with a transition in the molecule absorption occurs. This is then followed by the absorption of another photon that ionizes the molecule (Fig. 2.5). Thus, only molecules that are resonant with the laser and having a low-enough ionization potential can produce cations that can be detected by the microchannel plate of the TOF.

However, sometimes two photons of the same wavelength have insufficient collective energy to ionize the molecule, and thus another laser providing a higher energy photon is introduced to ionize the molecule – this is called two-color R2PI (2C-R2PI). 2C-R2PI has the added benefit of providing a ready means of minimizing saturation effects in the spectrum interrogated by the first laser. These saturation effects are sometimes unavoidably present in 1C experiments, but in 2C-R2PI the power of the laser used for the excitation step can be kept low, while the ionization step, which is non-resonant, can have its power increased to increase signal size. Furthermore, by simply changing which laser has its wavelength fixed and which is scanned, it is possible to determine the ionization potential of the analyte via a photoionization efficiency scan (PIE). A PIE scan is recorded by fixing the wavelength of the first photon on the lowest-energy transition from the ground state to the excited state, and then tuning the second photon until an onset of ion signal is observed. The sum of the two photons used is then the minimum energy required to ionize the molecule.

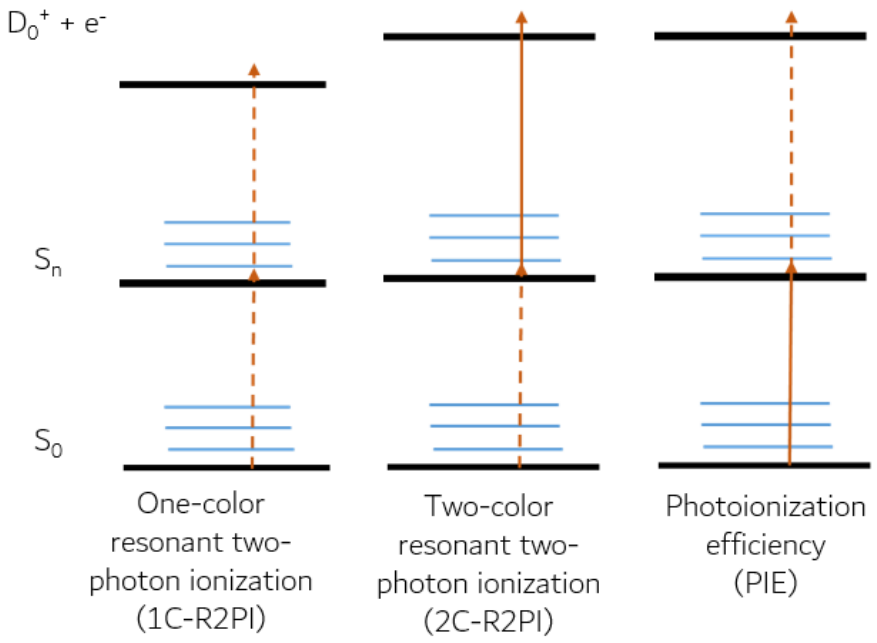


Figure 2.5 R2PI schemes

# CHAPTER 3. 3-PHENYL-2-PROPYNENITRILE

## 3.1 Background

As Titan's atmosphere is dominated by nitrogen gas, it would seem apt to have studies of any potentially relevant nitrogen-containing species. Nitriles are of specific interest because they are a simple way to begin incorporating nitrogen into the molecules already present in the atmosphere, and they could provide a source for biologically relevant nitrogen-containing compounds.

Many chemical species are known to exist in Titan's atmosphere, including cyanoacetylene, benzene, and diacetylene. Studies on the spectroscopy of and reactions between benzene and diacetylene have been published before.[1] Robinson et. al. were able to show that the primary product of this reaction, phenyldiacetylene, only exhibited broad transitions that were approximately 2,040 $cm^{-1}$ apart and attributed to a Franck-Condon progression involving the C≡C stretching mode. In an attempt to broaden the list of already-known nitrile species and better describe their photochemistry, we have undertaken the study of 3-phenyl-2-propynenitrile, as it is the likely product of a hypothesized reaction between benzene and UV-excited cyanoacetylene.[2]

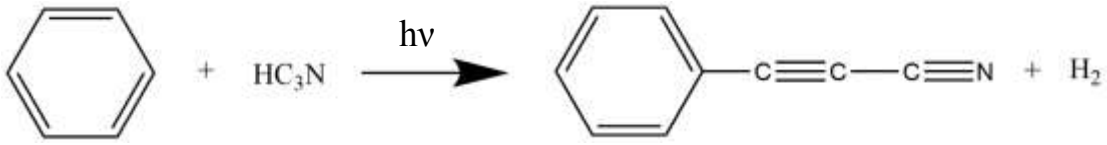

## 3.2 Methods

### 3.2.1 Experimental

The sample was purchased from Sigma-Aldrich at 98% purity.

The TOF-MS and fluorescence chambers were used to obtain the excitation and ground state spectra. The solid sample was placed in a Jordan valve (TOF-MS) or a general valve (fluorescence) with 500 μm orifice, entrained in 2.0 bar of He gas, and heated to 60°C. The excitation spectra were obtained by interrogating the supersonically-cooled sample with the tunable UV light from the frequency-doubled visible output of a Nd:YAG pumped dye laser (in 1C-R2PI and in LIF/DF). In 2C-R2PI, another photon overlapping in time and space with the first photon was introduced from an ArF excimer laser, which provided 2 mJ of 193 nm, or from a tunable solid state Continuum Horizon OPO set at 283 nm with 4 mJ of power.

PPN was also studied with CP-FTMW spectroscopy with the guidance of another graduate student in the group, Sean Fritz. The solid sample was put in a general valve with an 800 μm orifice, entrained in 1.4 bar of He gas, and heated to 55°C. The data was taken over the 8-18 GHz range, with 20 FIDs per gas pulse, and at 10% the power of the TWTA to reduce population transfer. 1.2 million averages were recorded, obtaining a signal-to-noise ratio of 312 on the strongest transition in the spectrum.

### 3.2.2 Calculations

Claudia Viquez-Rojas, a student in Professor Lyudmila Slipchenko's group at Purdue University, completed the electronic excited state calculations for this molecule. Ground and excited state geometries were optimized using the EOM-CCSD/cc-pVDZ level of theory in Q-Chem 4.4, while frequencies were calculated with B3LYP/6-311++G**. The multi-layer extension of the multi-configuration time dependent Hartree (ML-MCTDH) algorithm[3] was used to map the

potential energy surfaces of the first four excited states along each of the 39 normal modes. This was done by first performing normal mode walks, which involves displacing the equilibrium geometry along a normal mode vector with a stepsize of 0.5 dimensionless units. Along each point in the walk the lowest four excitation energies were calculated using EOM-CCSD/cc-pVDZ. The curves were fit with a second-degree polynomial to obtain kappa and gamma coupling values used in the vibronic Hamiltonian, while the third value, lambdas, were obtained from derivative couplings at the equilibrium geometry using Q-Chem 5.0. By this means, both first- and second-order vibronic coupling parameters, representing the interactions between vibrational and electronic levels, are obtained. ML-MCTDH was then used to propagate a wave-packet containing all or select normal modes. Two 300 fs runs were made, one starting in $S_1$ and the other starting in $S_2$, and a Fourier Transform of the autocorrelation function is used to predict the excitation and emission spectra of PPN.

Structure optimizations were also carried out with Gaussian 09[4] at the B2PLYPD3/aug-cc-pVTZ level to predict the ground state rotational constants for the microwave spectrum. A prediction of the spectrum at ~1 K for the 8-18 GHz region was then generated, and later used as a starting point for fitting the experimental spectrum using Pickett's SPFIT and SPCAT programs.[5]

## 3.3 Results

### 3.3.1 R2PI

A long 2C-R2PI scan from 292-208 nm (Fig. 3.1) was taken with the solid-state OPO as the scanned laser source and using the ArF excimer laser as the ionization photon. In this spectrum we can see a series of sharp peaks beginning with the origin at 35,261 $cm^{-1}$, followed by broad absorptions above 37,000 $cm^{-1}$. This suggests we have accessed the $S_1$ state in the sharp region, and perhaps reached another excited state once the broad absorptions begin.

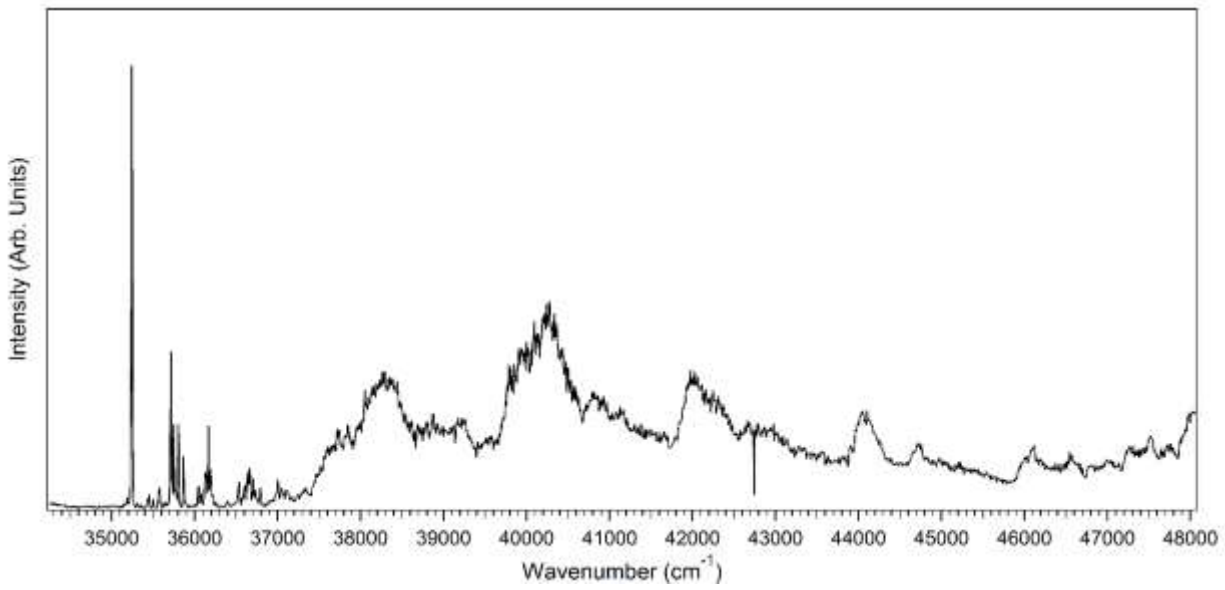


Figure 3.1 R2PI spectrum from 292-208 nm showing clear sharp peaks until ~37,000 $cm^{-1}$, followed by a series of broad absorptions. The dip at 42,735 $cm^{-1}$ is an artifact of the OPO.

The excitation spectrum was obtained in the TOF-MS chamber by both 1C- and 2C-R2PI. Although this means that the ionization potential of the molecule was low enough to allow two photons of the same wavelength to excite and ionize the molecule, the IP was not a value we could determine experimentally. This was due to the power of the ionization photon, which came from the Continuum OPO – the beam quality could not be maintained above 300 nm when lowering the power to a value where signal could not be seen.

For higher resolution 2C-R2PI, the doubled UV output of a dye laser was used as the first photon to obtain a rotational band contour (RBC) of the electronic origin at 35,261 $cm^{-1}$, as shown in Figure 3.2. This was taken in the hopes that it would allow the determination of the direction of the transition dipole moment (TDM), which would help elucidate which excited state was being accessed in the sharp region of the R2PI spectrum. Calculations at the EOM-CCSD/cc-pVDZ level of theory had predicted an excited state energy ordering in which the $S_0$-$S_1$ transition is a b-type transition, while the $S_0$-$S_2$ transition would be a-type. While both these transitions involve in-plane

TDMs, they are quite different from each other: the b-type TDM would describe a transition that is perpendicular to the $C_2$ axis, whereas the a-type TDM of the $S_0$-$S_2$ would describe a transition that is parallel to that same $C_2$ axis. Simulations to match the RBC using JB95 are pending.

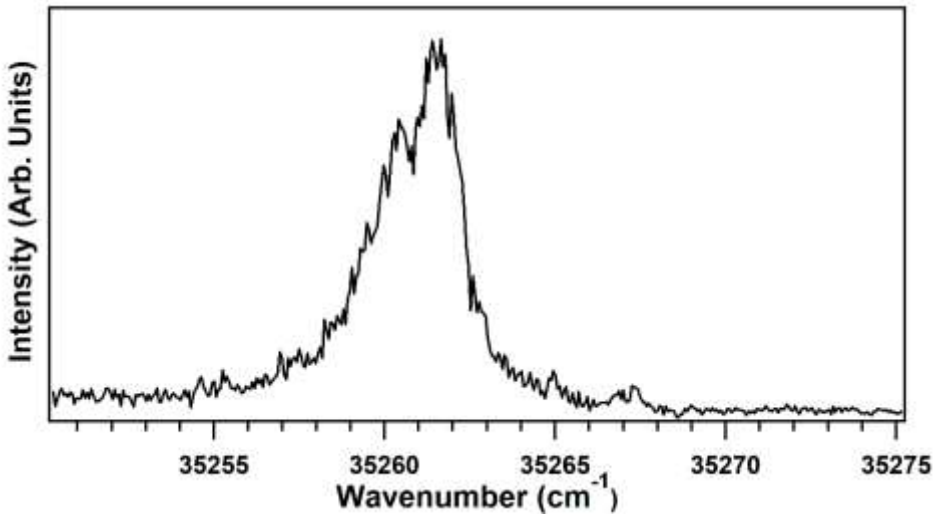


Figure 3.2 RBC of origin was not resolved enough to show if it were a transition to the $S_1$ or $S_2$ excited state.

To understand how long-lived this excited state is, we undertook a lifetime scan (Fig. 3.3) of the electronic origin in 2C-R2PI by scanning the delay between the excitation photon and the ionization photon. The scan clearly shows there is a very short-lived component which was just about the duration of the laser pulse at <10 ns, and a long-lived component of at least 800 ns. Only a lower-limit to the long-lived component could be obtained due to motion of the molecules along the expansion axis during the delay between the laser pulses.

The short-lived component is very likely the singlet excited state $S_1$, while the long-lived component is most likely a triplet state, accessed via intersystem crossing from the $S_1$. The ion retains the geometry of all the states discussed so far, in that the nitrile chain remains linear, so the triplet state, which is vibrationally hot, must absorb a photon of sufficient energy to ionize the molecule with $\Delta v=0$. The 193 nm photon provided by the excimer laser allows this.

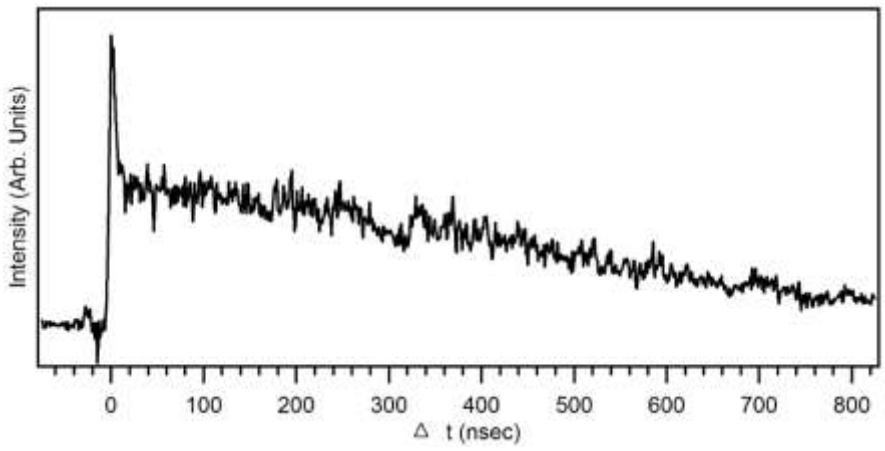


Figure 3.3 Duration of excited state as seen by ion signal as a function of delay between the excitation and ionization lasers, Δt. The signal is composed of two parts: a short-lived component less than 10 ns long, and a long-lived component of at least 800 ns.

### 3.3.2 Laser-induced Fluorescence

The LIF spectrum over the 35,200-36,630 $cm^{-1}$ region is shown in Figure 3.4, and reproduces the sharp region seen in the R2PI from Figure 3.1. The lifetime taken in LIF also showed that the fluorescing species is short, at less than 10 ns, making it likely the same state as the short-lived component seen in the R2PI lifetime scan. Fluorescence begins to die off above 36,050 $cm^{-1}$, in the same region where the broad peaks begin to appear in the R2PI spectrum. This suggests a non-radiative process takes over, perhaps internal conversion or intersystem crossing. We will return to the subject of the excited state processes in operation with this molecule in the discussion section.

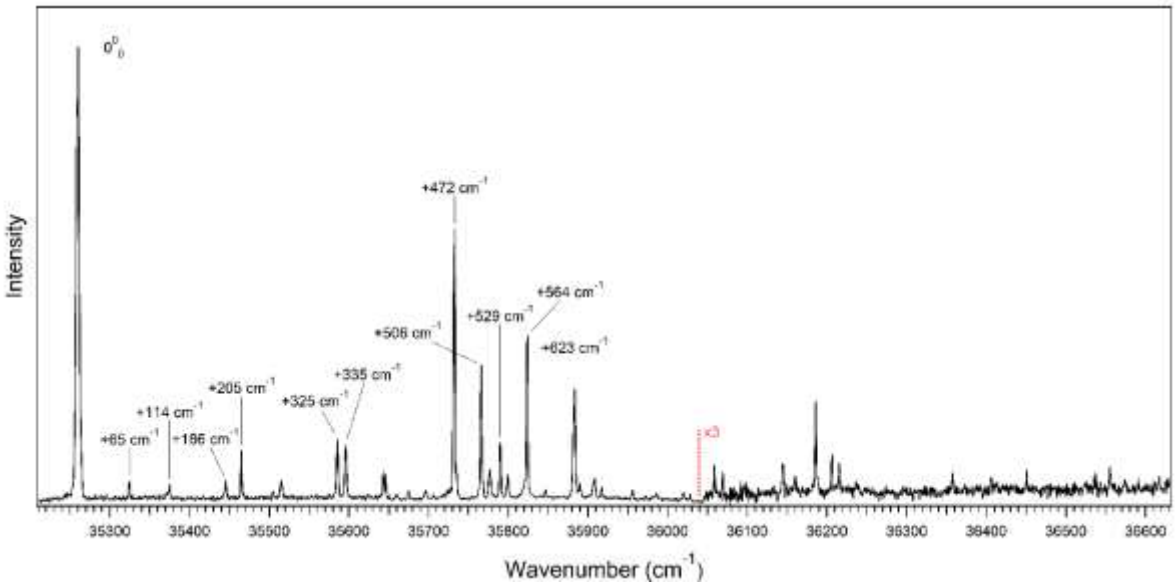


Figure 3.4 LIF excitation spectrum. Transitions for which DF spectra were obtained are labeled. The portion of the spectrum to the right of the red line had to increase by a factor of 3 in order to overlap properly with the rest of the spectrum.

### 3.3.3 Dispersed Fluorescence

Dispersed fluorescence spectra were taken with the excitation laser fixed on each of a total of twelve transitions in the LIF spectrum. These scans are shown in Figures 3.5-3.6.

Figure 3.5 shows all the DF scans, ranging from the origin to +623 cm$^{-1}$, and including both high- and low-intensity peaks. In all cases, the signal at 0 cm$^{-1}$ is the combined resonant fluorescence and scatter from the laser light, and is typically much larger in intensity than all the rest of the peaks in the DF scans. The next large peak to show up, in all but the origin DF spectrum, is the false origin peak. For example, a scan taken by sitting at the +205 cm$^{-1}$ transition in the excitation spectrum yields a DF spectrum with a false origin located at +209 cm$^{-1}$. The first value represents the excited state level, while the second represents the corresponding level in the ground state, showing they are different by only 4 cm$^{-1}$. In this way we are able to map out the ground state vibrational modes.

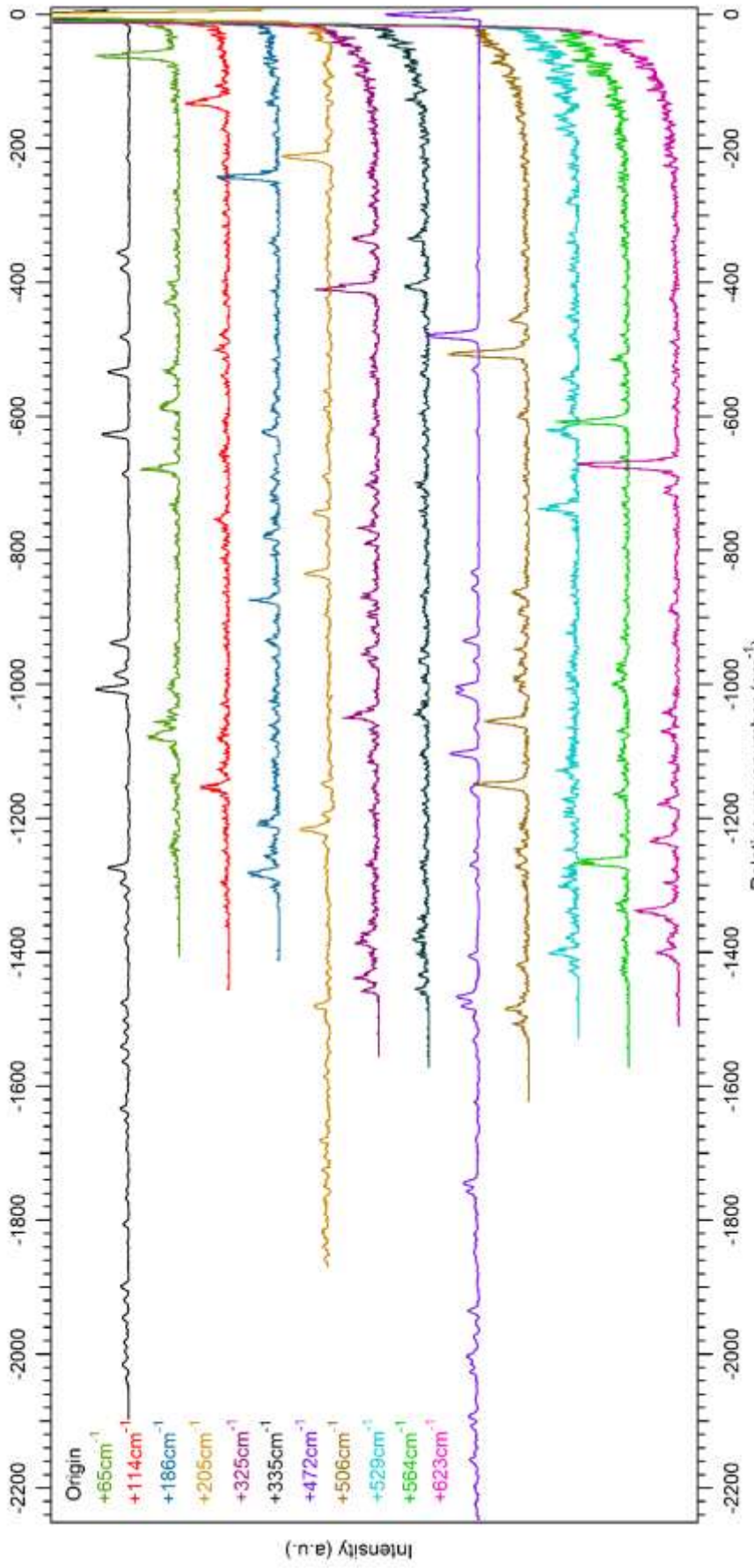


Figure 3.5 The 12 DF spectra taken on PPN.

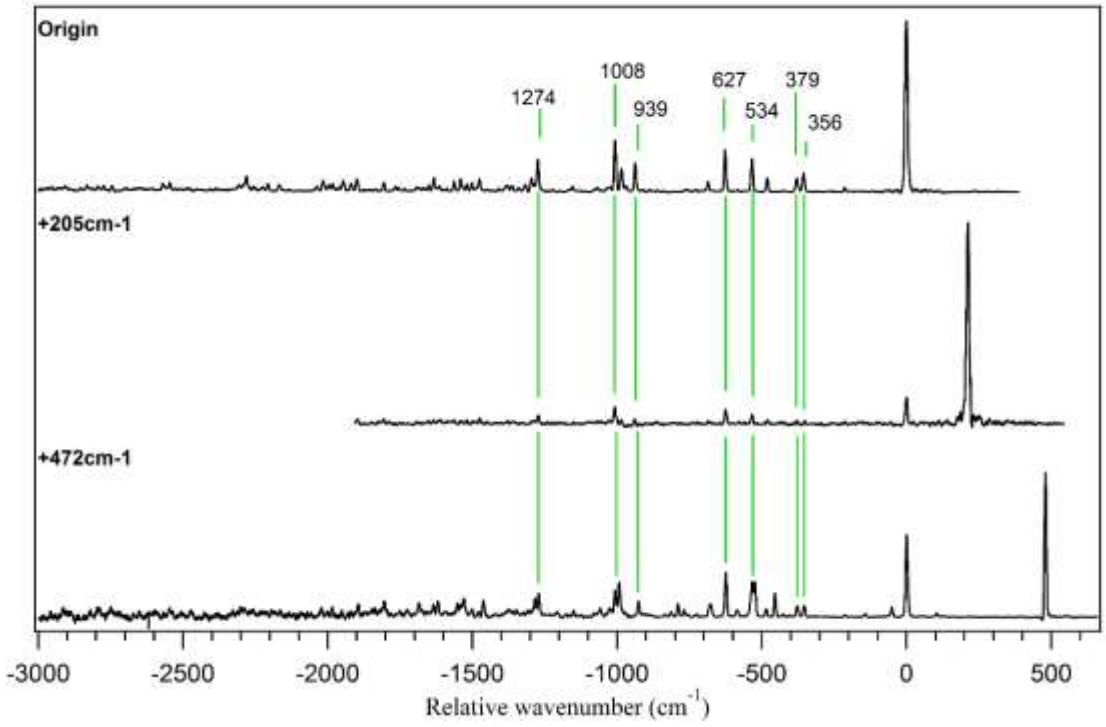


Figure 3.6 Dispersed fluorescence on the origin, +205, and +472 $cm^{-1}$ peaks. Spectra have been arranged such that the false origin in the +205 and +472 $cm^{-1}$ transitions are set to 0 $cm^{-1}$, and the wavenumber shift between scatter and false origin peaks are +209 and +479 $cm^{-1}$, respectively. Peaks are marked with green taglines to highlight the similarities between them.

Figure 3.6 is shown here to point out the similarities between the spectra. Indeed, this pattern of mirroring the origin's DF spectrum is true of all but the +529 $cm^{-1}$ transition, and adds to the argument that the ground and excited state share the same overall geometry.

### 3.3.4 EOM-CCSD and ML-MCTDH Calculations

Table 3.1 summarizes PPN's first four excited states calculated at the EOM-CCSD/cc-pVDZ level of theory and Figure 3.7 illustrates the orbitals involved in each transition. Note, first, that the $S_1$ is of $B_2$ symmetry but has an oscillator strength that is very small. Almost 0.5 eV higher in energy is a bright state, $S_2$ ($A_1$), with a large oscillator strength, and not too much higher are the

dark states $S_3$ and $S_4$ ($A_2$). Neither $S_1$ nor $S_2$ states show any change in the overall geometry of the molecule, which is consistent with the $\Delta v=0$ Franck-Condon factors seen in the spectra. Should there be any vibronic coupling, we expect certain vibrational modes to be important only if the product of that mode with the two excited states is the totally symmetric fundamental. For this molecule, then, we expect vibronic coupling to be allowed under these conditions: $a_1$ vibrational modes can only couple the $S_3$ and $S_4$ states; $a_2$ can couple $S_2$ and $S_3$, or $S_2$ and $S_4$; $b_1$ modes couple $S_1$ and $S_3$, or $S_1$ and $S_4$; and, finally, $b_2$ modes couple $S_1$ and $S_2$.

Table 3.1 Summary of first four excited states calculated with the EOM-CCSD/cc-pVDZ level of theory.

| Excited State | Symmetry | Oscillator strength | Vertical excitation energy (eV) |
|---|---|---|---|
| $S_1$ | $B_2$ | 0.003 | 4.922 |
| $S_2$ | $A_1$ | 0.361 | 5.485 |
| $S_3$ | $A_2$ | 0 | 5.562 |
| $S_4$ | $A_2$ | 0 | 5.790 |

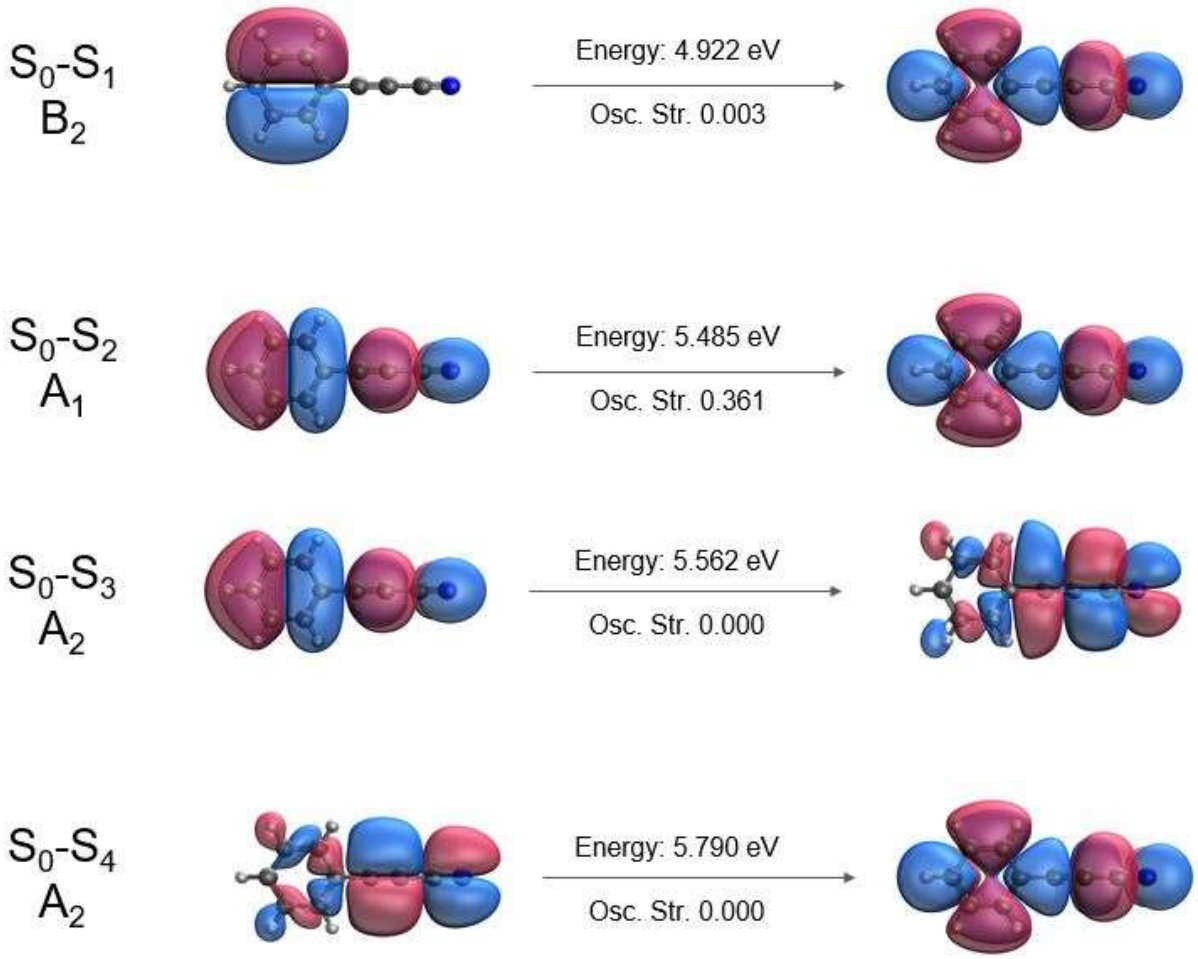


Figure 3.7 Orbital representations of the transitions from the ground to the first four excited states. The symmetry label on the left corresponds to the symmetry of the excited state.

The calculated lambda parameters used in the ML-MCTDH indicate that $b_2$ vibrational modes strongly couple the $S_1$ and $S_2$ states, and $b_1$ modes couple $S_1$ with both $S_3$ and $S_4$. A propagation of the $S_1$ state using only ten normal modes – those that showed strong coupling as well as mode 36 (though it was not predicted to have any coupling) – is shown in Figure 3.8 against the LIF spectrum. Features are broadened due to the short propagation time of 300 fs, and while activity is generally in the same area as that seen in the LIF, the intensity pattern has not been reproduced. This is especially true for the second most intense peak in the LIF, the +472 $cm^{-1}$

transition, which is bounded on both sides by small transitions from the simulation. In fact, the second most intense peak in the simulation is at higher energy, near 36,280 $cm^{-1}$. The transition lower in energy than the origin may be a hot band.

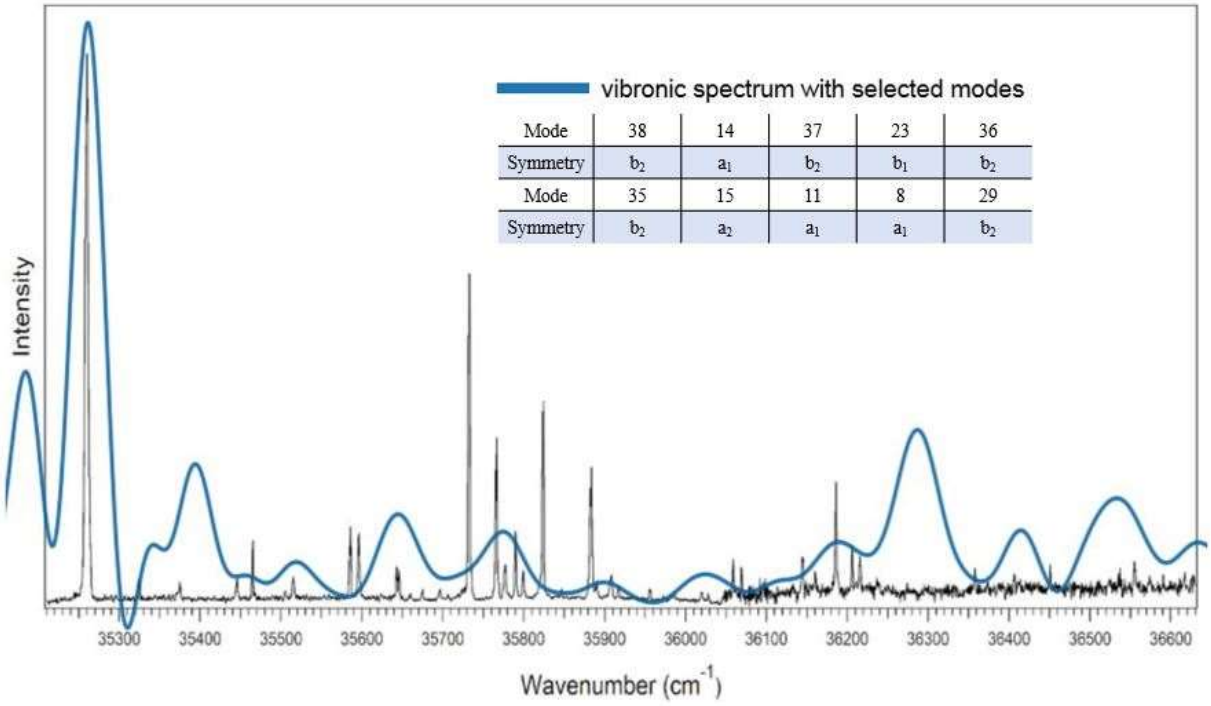


Figure 3.8 The predicted excitation spectrum (blue) overlaying the experimental LIF spectrum (black) using normal modes that showed strong couplings between states.

### 3.3.5 Microwave

PPN is a near-prolate symmetrical top, having all its dipole moment along the a-axis (5.9D), thus allowing for the observation of only a-type transitions. A total of 33 transitions were assigned using SPFIT and SPCAT, with a standard deviation in the fit of 38 kHz. The predicted transitions are plotted in blue against the 1.2M average experimental spectrum in Figure 3.9. Hyperfine splittings were not observed in the experimental spectrum, as predictions showed they were below the resolution of the instrument (62.5 kHz for a 16 μs FID collection time). A summary of the

experimental and calculated rotational parameters for PPN are shown in Table 3.2, and a list of the assigned transitions are shown in Table 3.3.

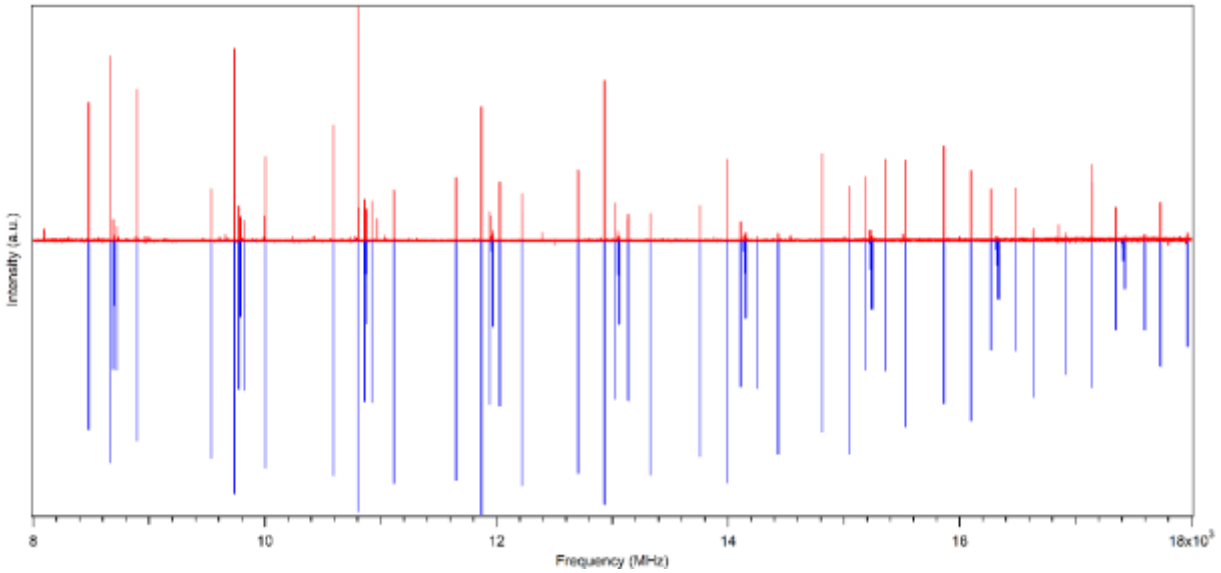


Figure 3.9 Experimental microwave data over the 8-18 GHz region shown in red, predictions shown in blue.

Table 3.2 Summary of experimental and predicted PPN properties.

| | Experimental | Calculation[a] |
|---|---|---|
| A (MHz) | 5660.31(66) | 5,698 |
| B (MHz) | 569.5773(10) | 571.4 |
| C (MHz) | 517.4027(10) | 519.4 |
| $\kappa$[b] | -0.98 | -0.98 |
| $\lvert\mu_a\rvert$[c] (D) | 100% | 5.9 |
| $\lvert\mu_b\rvert$[c] (D) | -- | 0.0 |
| $\lvert\mu_c\rvert$[c] (D) | -- | 0.0 |
| $\lvert\mu_T\rvert$[c] (D) | -- | 5.9 |
| $\chi_{aa}$[d] (MHz) | -- | 1.22 |
| $\chi_{bb}$[d] (MHz) | -- | -3.31 |
| $\chi_{cc}$[d] (MHz) | -- | 2.09 |

[a] B2PLYPD3/aug-cc-pVTZ

[b] Ray's asymmetry parameter, $\kappa=(2B-A-C) / (A-C)$

[c] $\lvert\mu_a\rvert$, $\lvert\mu_b\rvert$, $\lvert\mu_c\rvert$, and $\lvert\mu_T\rvert$ are the absolute values of the dipole moment components along the a, b, and c axes, and the total dipole moment.

[d] $\chi_{aa}$, $\chi_{bb}$, and $\chi_{cc}$ are the $^{14}N$ nuclear quadrupole coupling constants

Table 3.3 Summary of assigned transitions.

| $\upsilon_{obs}$ (MHz) | Assignment ($J'_{Ka'Kc'}$-$J''_{Ka''Kc''}$) | OMC[a] (MHz) | $\upsilon_{obs}$ (MHz) | Assignment ($J'_{Ka'Kc'}$-$J''_{Ka''Kc''}$) | OMC[a] (MHz) |
|---|---|---|---|---|---|
| 8,479.438 | $8_{1,8}$ -$7_{1,7}$ | 0.032 | 12,704.688 | $12_{1,12}$ -$11_{1,11}$ | 0.037 |
| 8,662.563 | $8_{0,8}$ -$7_{0,7}$ | 0.040 | 12,932.875 | $12_{0,12}$-$11_{0,11}$ | 0.001 |
| 8,691.000 | $8_{2,7}$ -$7_{2,6}$ | 0.031 | 13,025.750 | $12_{2,11}$-$11_{2,10}$ | -0.073 |
| 8,724.313 | $8_{2,6}$ -$7_{2,5}$ | 0.029 | 13,046.125 | $12_{9,3}$-$11_{9,2}$ | 0.043 |
| 8,896.375 | $8_{1,7}$-$7_{1,6}$ | 0.058 | 13,060.750 | $12_{3,9}$-$11_{3,8}$ | -0.069 |
| 9,536.938 | $9_{1,9}$-$8_{1,8}$ | -0.010 | 13,136.625 | $12_{2,10}$-$11_{2,9}$ | -0.037 |
| 9,735.438 | $9_{0,9}$-$8_{0,8}$ | 0.053 | 13,327.000 | $12_{1,11}$-$11_{1,10}$ | 0.057 |
| 9,775.688 | $9_{2,8}$-$8_{2,7}$ | 0.044 | 13,758.750 | $13_{1,13}$-$12_{1,12}$ | 0.022 |
| 9,786.563 | $9_{4,6}$-$8_{4,5}$ | -0.071 | 13,991.063 | $13_{0,13}$ -$12_{0,12}$ | -0.001 |
| 9,789.000 | $9_{3,7}$-$8_{3,6}$ | -0.040 | 14,107.688 | $13_{2,12}$-$12_{2,11}$ | -0.033 |
| 9,789.875 | $9_{3,6}$-$8_{3,5}$ | -0.046 | 14,247.313 | $13_{2,11}$-$12_{2,10}$ | 0.001 |
| 9,823.063 | $9_{2,7}$-$8_{2,6}$ | -0.008 | 14,431.313 | $13_{1,12}$-$12_{1,11}$ | 0.005 |
| 10,005.688 | $9_{1,8}$-$8_{1,7}$ | 0.045 | 14,811.813 | $14_{1,14}$-$13_{1,13}$ | -0.017 |
| 10,593.750 | $10_{1,10}$-$9_{1,9}$ | 0.038 | 15,045.313 | $14_{0,14}$-$13_{0,13}$ | -0.018 |
| 10,804.938 | $10_{0,10}$-$9_{0,9}$ | 0.049 | 15,188.750 | $14_{2,13}$-$13_{2,12}$ | -0.010 |
| 10,859.688 | $10_{2,9}$-$9_{2,8}$ | -0.030 | 15,361.000 | $14_{2,12}$-$13_{2,11}$ | -0.004 |
| 10,871.938 | $10_{7,3}$-$9_{7,2}$ | 0.085 | 15,534.063 | $14_{1,13}$-$13_{1,12}$ | 0.039 |
| 10,877.938 | $10_{3,8}$-$9_{3,7}$ | -0.056 | 15,863.938 | $15_{1,15}$ -$14_{1,14}$ | -0.003 |
| 10,879.438 | $10_{3,7}$ -$9_{3,6}$ | -0.043 | 16,095.750 | $15_{0,15}$ -$14_{0,14}$ | 0.000 |
| 10,924.625 | $10_{2,8}$ -$9_{2,7}$ | 0.002 | 16,268.813 | $15_{2,14}$-$14_{2,13}$ | -0.072 |
| 11,114.000 | $10_{1,9}$ -$9_{1,8}$ | 0.045 | 16,477.563 | $15_{2,13}$ -$14_{2,12}$ | -0.033 |
| 11,649.625 | $11_{1,11}$-$10_{1,10}$ | -0.001 | 16,634.875 | $15_{1,14}$-$14_{1,13}$ | -0.010 |
| 11,870.813 | $11_{0,11}$-$10_{0,10}$ | 0.033 | 16,915.063 | $16_{1,16}$ -$15_{1,15}$ | 0.019 |
| 11,943.125 | $11_{2,10}$-$10_{2,9}$ | -0.010 | 17,142.438 | $16_{0,16}$ -$15_{0,15}$ | -0.038 |
| 11,967.313 | $11_{3,9}$ -$10_{3,8}$ | -0.055 | 17,347.938 | $16_{2,15}$ -$15_{2,14}$ | -0.069 |
| 11,969.750 | $11_{3,8}$ -$10_{3,7}$ | -0.060 | 17,596.875 | $16_{2,14}$ -$15_{2,13}$ | 0.015 |
| 12,029.125 | $11_{2,9}$ -$10_{2,8}$ | 0.010 | 17,733.750 | $16_{1,15}$-$15_{1,14}$ | 0.021 |
| 12,221.125 | $11_{1,10}$-$10_{1,9}$ | 0.020 | 17,965.125 | $17_{1,17}$ -$16_{1,16}$ | 0.003 |

[a] OMC = $\nu_{obs} - \nu_{calc}$

## 3.4 Discussion

The R2PI spectrum of 3-phenyl-2-propynenitrile taken over the 292-208 nm range exhibited sharp features at the low energy end of the spectrum, followed by a switch to broad absorptions below 270 nm (above 37,000 $cm^{-1}$), initially suggesting we had access to both $S_1$ (in the sharp portion) and $S_2$ (in the broad portion). However, DFT calculations state we are unlikely to see the $S_1$ state (Table 3.1), as the $S_1$ ($^1B_2$) ← $S_0$ ($^1A_1$) is weak, having an extremely low oscillator strength; on the other hand, the $S_2$ ($^1A_1$) ← $S_0$ ($^1A_1$) is bright with a large oscillator strength. The excitation spectra indicate an upper state which has a similar geometry to the ground state, which fits with the optimized geometry results of both the $S_1$ and $S_2$. Many of the DFL spectra also indicate the molecule's excited state geometry is nearly identical to that of the ground state: the DFL spectra are near mirror images of the excitation spectrum – albeit with different intensity patterns – built off false origins, with their most intense transitions associated with $\Delta v=0$ Franck-Condon factors.

The DF spectra have also allowed us to understand the frequency changes in vibrational modes between ground and excited state via the false origins: the wavenumber position in the excitation spectrum relative to the origin provides the excited state frequency of a particular transition, while the false origins out of that level provide the corresponding ground state level. Those values have been summarized in Table 3.4. It should be pointed out that all the transitions for which DF spectra were taken are of modes having either $b_1$ or $b_2$ symmetry, except for the origin and +335 $cm^{-1}$ transitions, which are $a_1$. Another point to make is that several of the modes show dramatic frequency changes between ground and excited state: for example, when we pump the +186 $cm^{-1}$ from the excitation spectrum, the molecule fluoresces down into a level that is +245 $cm^{-1}$ above the zero-point level. Indeed, this is true for when we pump the +325, 335, 564, and 623 $cm^{-1}$ transitions.

Table 3.4 Assignments for the $0^0_0$ DF transitions. The values in parentheses in the last column indicate the peak chosen to disperse from the excitation spectrum.

| Assignment | B3LYP/6-311++G** $S_0$ frequency ($cm^{-1}$) | Symmetry | Origin DF frequency ($cm^{-1}$) | DF false origins ($cm^{-1}$) |
|---|---|---|---|---|
| | 70 | $b_2$ | | 62 (65) |
| | 75 | $b_1$ | | 135 (114) |
| | 192 | $b_1$ | | 245 (186) |
| $38^0_1$ | 211 | $b_2$ | 210 | 210 (205) |
| $24^0_1$ | 363 | $b_1$ | 354 | 412 (325) |
| $14^0_1$ | 366 | $a_1$ | 377 | 408 (335) |
| | 402 | $a_2$ | | |
| $37^0_1$ | 489 | $b_2$ | 479 | 480 (472) |
| | 503 | $b_1$ | | 509 (506) |
| | 524 | $b_1$ | | 544 (529) |
| $36^0_1$ | 538 | $b_2$ | 532 | 608 (564) |
| $35^0_1$ | 630 | $b_2$ | 625 | 671 (623) |
| | 659 | $b_1$ | | |
| $13^0_1$ | 694 | $a_1$ | 684 | |
| | 759 | $b_1$ | | |
| | 866 | $a_2$ | | |
| $19^0_1$ | 934 | $b_1$ | 937 | |
| | 970 | $a_1$ | | |
| | 981 | $a_2$ | | |
| $18^0_1$ | 986 | $b_1$ | 984 | |
| $11^0_1$ | 1016 | $a_1$ | 1006 | |
| | 1058 | $a_1$ | | |
| | 1106 | $b_2$ | | |
| | 1174 | $b_2$ | | |
| | 1200 | $a_1$ | | |
| $8^0_1$ | 1299 | $a_1$ | 1272 | |
| $32^0_1$ | 1306 | $b_2$ | 1294 | |

The rotational band contour (Fig. 3.2) spectrum, obtained to identify the excited state, did not have a high enough resolution from the dye laser to distinguish between a- and b-type rotational band profiles. However, given that there are similarities in structure between PPN and phenylacetylene, which proved to have a b-type origin band,[6] it's quite probable that PPN's origin band could be b-type as well, especially since there are some similarities in the profile. If the

simulations help support this, we could thus identify this transition as the $S_1$ ($^1B_2$) ← $S_0$ ($^1A_1$) transition. Additionally, in making assignments in the origin DF spectrum we notice a preponderance of $b_2$ symmetry fundamentals (Fig. 3.10) that are inconsistent with an $S_2$ ($^1A_1$) ← $S_0$ ($^1A_1$), but in keeping with vibronically-induced bands that couple the $S_1(B_2)$ state with $S_2(A_1)$. The most notable of these fundamentals involves the $37^1_0$ band (+472 $cm^{-1}$), the second most intense band of the excitation spectrum, though it is much smaller in the origin DF spectrum. A list of the calculated and experimental values (Table 3.4) shows quite clearly that the assignments were mostly made out of necessity, especially in the low-frequency modes as there were very few totally symmetric vibrations available to choose from.

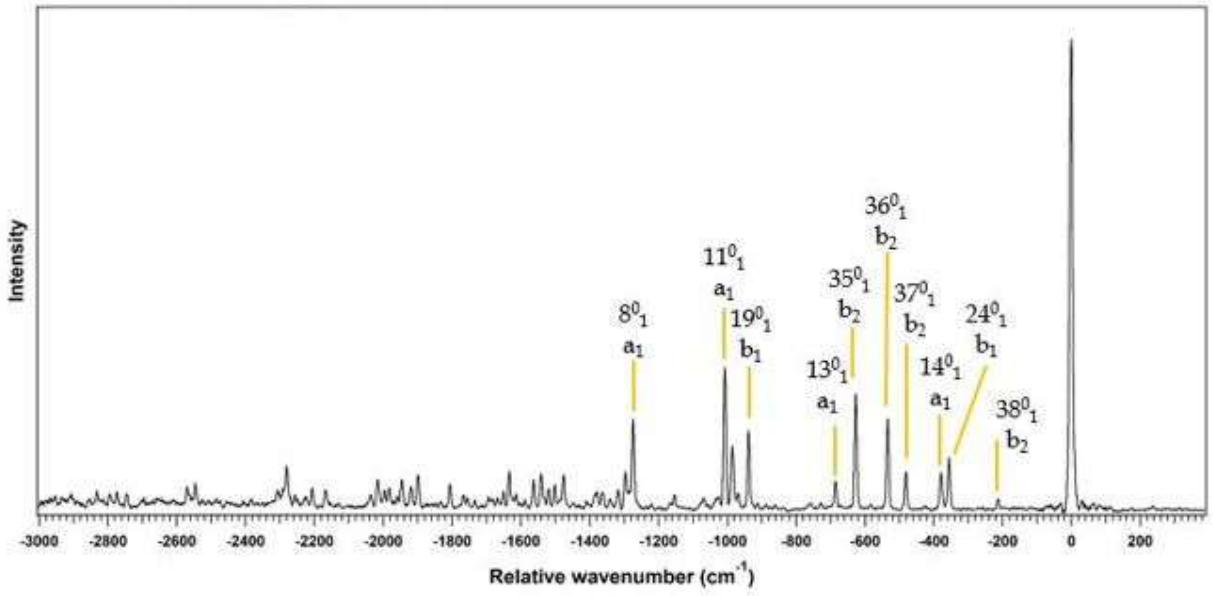


Figure 3.10 Origin DF spectrum with some vibrational mode assignments and their corresponding symmetries.

In addition, the ML-MCTDH was able to partially reproduce the excitation spectrum when it considered the modes that, in general, showed coupling between electronic states (Fig. 3.8). Such strong coupling between the states is in keeping with our assignment of the spectrum to the weakly allowed $S_1$ state, which is picking up intensity from $S_2$ via vibronic coupling involving $b_2$ symmetry vibrations.

It is interesting and a bit puzzling that, in addition to the $b_2$ fundamentals in the DF spectra, there is also activity in select out-of-plane $b_1$ fundamentals, something that is seemingly inconsistent with a ππ* transition with an in-plane transition dipole moment. As with the $b_2$ fundamentals, most of the $b_1$ assignments were made out of necessity. These $b_1$ fundamentals could gain intensity through one of two mechanisms. In the first case (Fig. 3.11a), perhaps higher-order Herzberg-Teller terms could be involved in the vibronic coupling. For instance, $a_2$ fundamentals in the $S_2$ ($A_1$) state could be mixing with $a_1$ levels in the $S_4$ ($A_2$) state. These intermediate levels in $S_4$ then mix in turn with $b_1$ fundamentals in $S_1$ ($B_2$). However, the simple fact is that $a_2$ fundamentals in $S_2$ ($A_1$) are no more allowed from the $S_0$ ($A_1$) zero-point level than are $b_1$ fundamentals in $S_1$ ($B_2$).

The second explanation, shown schematically in Figure 3.11b, involves a combination of Coriolis coupling and vibronic coupling: the $b_1$ states we see in the spectra are typically part of a $b_1/b_2$ vibrational pair, such that the first is the out-of-plane bending of the nitrile chain and the other is the corresponding in-plane bending (Fig. 3.12). If these modes were degenerate, an appropriate choice of phase would produce vibrational angular momentum about the ‘a’ axis (‘z’ axis). Coriolis coupling is a form of vibration-rotation coupling that arises from perturbation terms in the Hamiltonian that transform as rotations about the x-, y-, and z-axes: $R_x$, $R_y$, or $R_z$. In the $C_{2v}$ point group, these transform as $b_2$, $b_1$, and $a_2$, respectively. So Coriolis coupling about the ‘z’ axis

would mix vibrational levels of symmetry $b_1$ with those of symmetry $b_2$. Since the $b_1/b_2$ pairs are close in frequency, it is at least plausible that these pairs would undergo efficient Coriolis mixing, producing some $b_2$ symmetry vibrational character to the $b_1$ fundamentals, and therefor enabling the $b_1$ fundamentals to gain intensity via the same first-order vibronic coupling involving $S_1/S_2$.

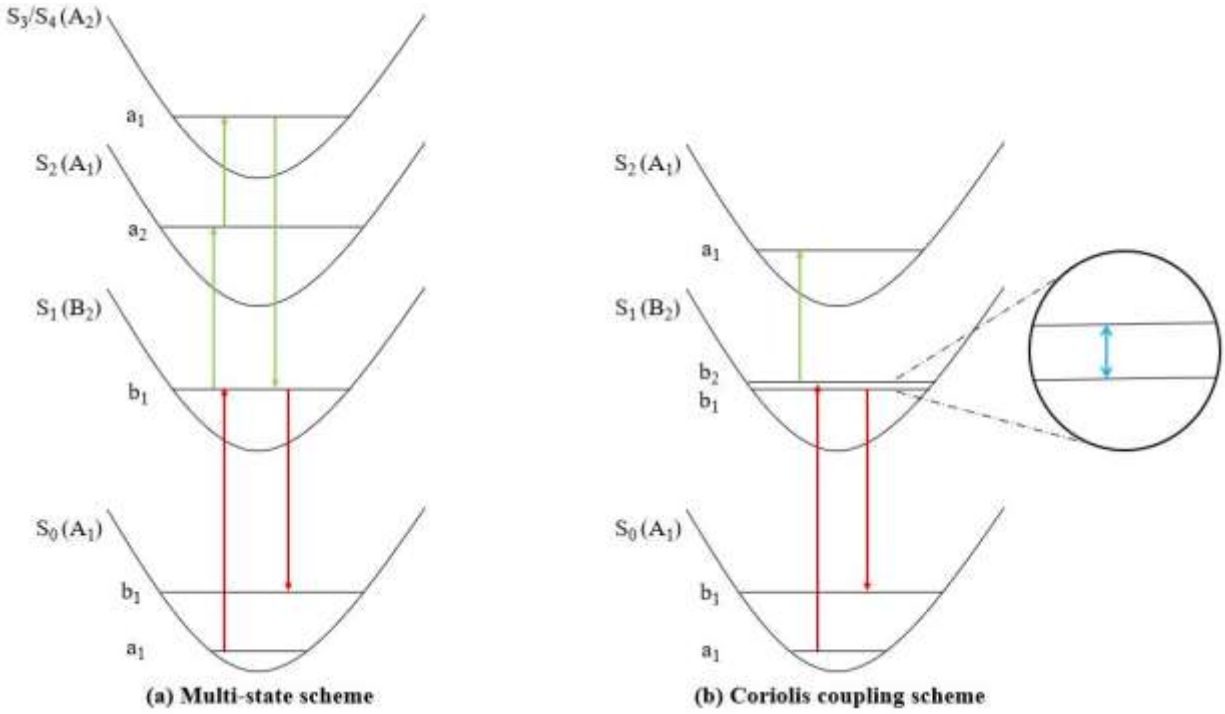


Figure 3.11 Excitation and fluorescence are shown with red arrows, vibronic coupling in green, and Coriolis coupling in blue. Scheme (a) represents the multi-state method for lighting up the $b_1$ vibrational modes, while (b) represents the Coriolis coupling method.

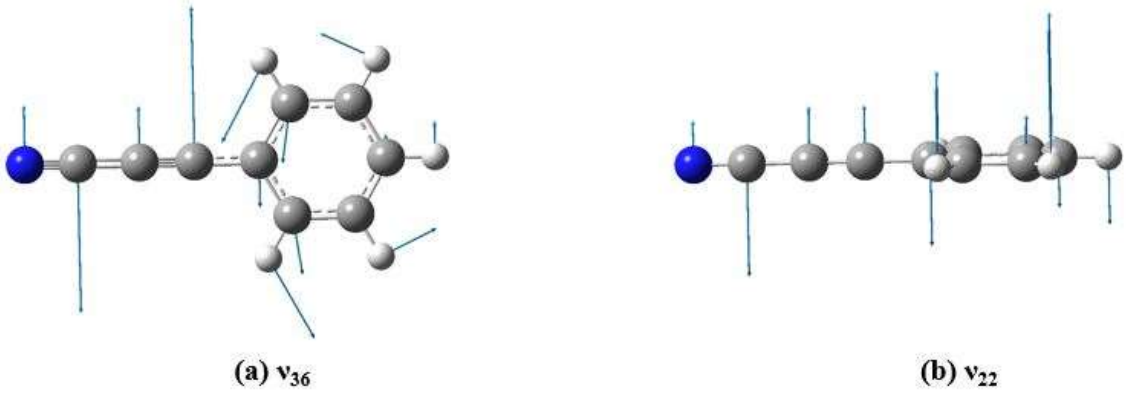


Figure 3.12 Pictorial representation of a ground state $b_1/b_2$ vibrational pair. (a) $\nu_{36}$ is the in-plane $b_2$ vibration calculated to be at +538 $cm^{-1}$ while (b) $\nu_{22}$ is the corresponding out-of-plane $b_1$ vibration at +524 $cm^{-1}$. DFT (B3LYP/6-311++G**) was used to calculate the harmonic frequencies.

Finally, the excited state lifetime of the long-lived component puts PPN in the same standing as the similar molecules benzonitrile and phenylacetylene.[6-7] Both molecules exhibited very short-lived singlet excited states in both fluorescence and pump-probe ionization studies similar to our own. Each molecule also had a much longer-lived ( > 150 μsec) component attributed to the lowest triplet state[6, 8-9] that was only produced during the laser pulse. Johnson et. al. had proposed that strong coupling between singlet excited states after the absorption of two photons creates a mixed state that is isoenergetic with the triplet manifold. This mixed state can then undergo stimulated emission to the triplet manifold.[9] Although we have no evidence for the presence of a triplet state besides the long-lived component of the excited state lifetime, we do know this component is not present in the fluorescence experiments.

## 3.5 Conclusion

The UV spectroscopy of PPN has shown sharp, bright features above 270 nm attributed to the weakly-allowed $S_1$ ($^1B_2$) ← $S_0$ ($^1A_1$) electronic transition. The evidence from excited state spectra (R2PI and LIF) as well as the ground state spectra (DF) indicates strong vibronic coupling is involved in producing so many $b_1$ and $b_2$ vibrations. Strong vibronic coupling between $S_1$ and $S_2$ is also needed to partially reproduce the excited state spectrum using the ML-MCTDH algorithm. The $b_2$ modes are rather simple to explain, as they would involve vibronic coupling between the $S_1$ ($^1B_2$) and $S_2$ ($^1A_1$) electronic states. However, the presence of so many $b_1$ fundamentals is more complicated: they are most likely the result of Coriolis coupling between $b_1$ and $b_2$ levels, should those levels be nearby in energy and the out-of-plane and in-plane vibrational equivalents of each other.

## 3.6 References


1. Robinson, A.G., et. al., J. Phys. Chem. A., 2000. **104**: 10312-10320.
2. Krasnopolsky, V.A., Icarus, 2009. **201**: p. 226-256.
3. The MCTDH Package, Version 8.2, G.A. Worth, M.H. Beck, A. Jäckle, and H.-D. Meyer. University of Heidelberg, Heidelberg, Germany, 2000. H.-D. Meyer, Version 8.3, 2002, Version 8.7, 2007.
4. Gaussian 09, R.B., D.01, M. J. Frisch, G. W. Trucks, H. B. Schlegel, G. E. Scuseria, M. A. Robb, J. R. Cheeseman, G. Scalmani, V. Barone, B. Mennucci, G. A. Petersson, H. Nakatsuji, M. Caricato, X. Li, H. P. Hratchian, A. F. Izmaylov, J. Bloino, G. Zheng, J. L. Sonnenberg, M. Hada, M. Ehara, K. Toyota, R. Fukuda, J. Hasegawa, M. Ishida, T. Nakajima, Y. Honda, O. Kitao, H. Nakai, T. Vreven, J. A. Montgomery, Jr., J. E. Peralta, F. Ogliaro, M. Bearpark, J. J. Heyd, E. Brothers, K. N. Kudin, V. N. Staroverov, T. Keith, R. Kobayashi, J. Normand, K. Raghavachari, A. Rendell, J. C. Burant, S. S. Iyengar, J. Tomasi, M. Cossi, N. Rega, J. M. Millam, M. Klene, J. E. Knox, J. B. Cross, V. Bakken, C. Adamo, J. Jaramillo, R. Gomperts, R. E. Stratmann, O. Yazyev, A. J. Austin, R. Cammi, C. Pomelli, J. W. Ochterski, R. L. Martin, K. Morokuma, V. G. Zakrzewski, G. A. Voth, P. Salvador, J. J. Dannenberg, S. Dapprich, A. D. Daniels, O. Farkas, J. B. Foresman, J. V. Ortiz, J. Cioslowski, and D. J. Fox, Gaussian, Inc., Wallingford CT, 2010, 2013.
5. Pickett, H.M., J. Mol. Spectrosc., 1991. **377**: 371–377.

6. Ribblett, J.W., et. al., J. Chem. Phys. 1999. **111**: 8454-8461.
7. Hofstein, J., et. al., J. Phys. Chem. A. 2008. **112**: 1195-1201.
8. Johnson, P.M., and T.J. Sears, J. Phys. Chem. 2013. **117**: 7786-7793.
9. Johnson, P.M., and T.J. Sears, J. Chem. Phys. 2015. **143**: 044305.

# CHAPTER 4. METHYLATED DERIVATIVES OF 3-PHENYL-2-PROPYNENITRILE

## 4.1 Introduction

Since 3-phenyl-2-propynenitrile might very well exist in Titan's atmosphere as the photochemical product of benzene and cyanoacetylene, it is quite likely that another molecule present on Titan, toluene, could very well react with cyanoacetylene as well. The products in that case would be the *ortho*-, *meta*-, and *para*-methyl PPN.

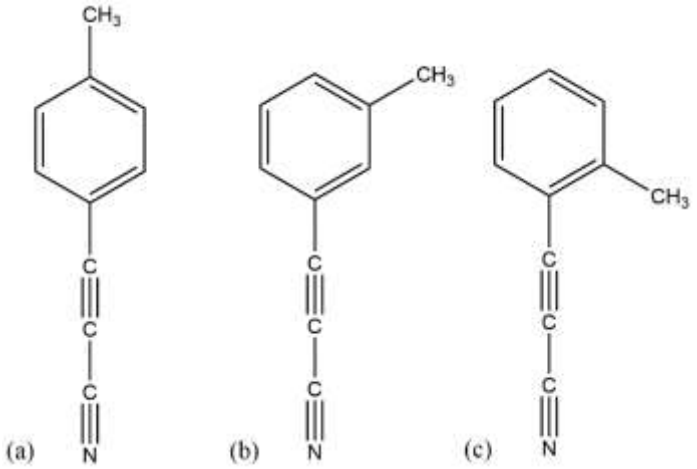


Figure 4.1 (a) *p*-methyl PPN, (b) *m*-methyl PPN, and (c) *o*-methyl PPN.

As the spectroscopic assignments of PPN proved difficult to pin down, we decided that adding the methyl group, which exhibits a torsional barrier that is sensitive to the local environment, might help clear up the assignments. In the case of PPN, the ground state and both $S_1$ and $S_2$ were $C_{2v}$ symmetry. The methylated PPN would prove simpler because all but the *p*-methyl PPN were now $C_s$ symmetry, which simplifies the spectroscopy by leaving only two options for assignments: in-plane (a') and out-of-plane modes (a").

## 4.2 Methods

### 4.2.1 Experimental

Samples of each compound were synthesized by Dr. Anthony Tomaine and Joseph Bungard.[1] For the R2PI scans, the samples were placed in the Jordan valve. The *p*- and *m*-methyl PPN were heated to 70°C, while the *o*-methyl PPN was heated to 75°C. 2C-R2PI was accomplished using the doubled UV output of a Nd:YAG pumped dye laser for the excitation photon, followed by the ionization photon from a solid-state Continuum Horizon OPO providing 1 mJ of 250 nm. The full overview scans from 293-238 nm were taken with 1C-R2PI using the Horizon OPO with a power of about 4 mJ. For the LIF and DF experiments, the samples were placed in a general valve and heated about 5°C higher than in the TOF/MS setup. The spectra were obtained using the doubled output of the Nd:YAG pumped dye laser.

### 4.2.2 Calculations

Density functional theory (DFT) and time-dependent density functional theory (TD-DFT) were used to optimize the geometries of and calculate harmonic frequencies for the $S_0$ ground, $S_1$, and $S_2$ excited states of all methylated PPN molecules. Gaussian 09[2] was used with the ωB97XD level of theory and 6-31+G(d) basis set.

## 4.3 Results

As with the PPN, the calculations for all three methylated PPN molecules show that the $S_2$ ($^1$A') ← $S_0$ ($^1$A') transition carries significant oscillator strength, while the $S_1$ ($^1$A') ← $S_0$ ($^1$A') does not, although in these cases the $S_1$ is significantly – and unreasonably – lower in energy than the $S_2$ state (Table 4.1). Figure 4.2 reproduces the geometries of each of the first three singlet states in each molecule, and we see that the $S_1$ excited state shows a bending in the nitrile chain relative

to either the ground or second excited state. However, this level of theory is notorious for getting the wrong energy ordering and geometry of the excited states, so we are currently running the calculations as we did with PPN, using EOM-CCSD/cc-pVDZ.

Table 4.1 Summary of the calculated energies and oscillator strengths for transitions from the ground state.

| | $S_1$ | | $S_2$ | |
|---|---|---|---|---|
| | Energy[a] (eV) | Oscillator Strength | Energy[a] (eV) | Oscillator Strength |
| *o*-methyl PPN | 1.99 | 0.0020 | 3.94 | 0.2567 |
| *m*-methyl PPN | 2.00 | 0.0020 | 3.97 | 0.2615 |
| *p*-methyl PPN | 1.96 | 0.0019 | 3.96 | 0.3217 |

[a] Vertical excitation energy

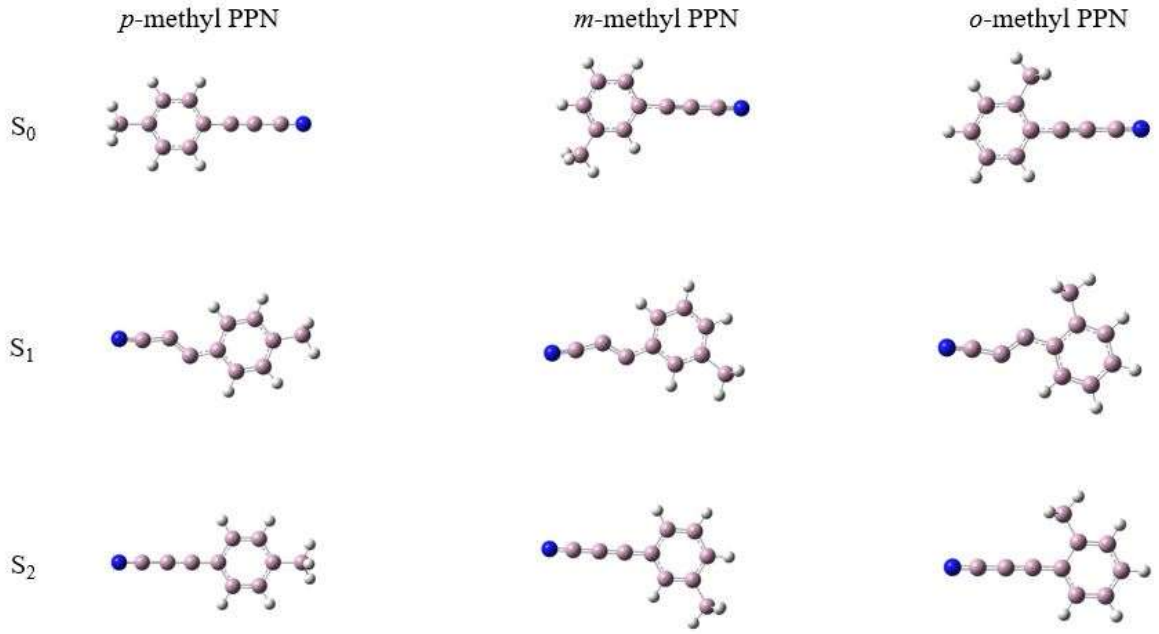


Figure 4.2 The optimized geometries of the ground and first two excited states for *p*-, *m*-, and *o*-methyl PPN.

The 1C-R2PI overview scans of all three molecules are shown in Figure 4.3. Once again, sharp features appear in the low-frequency end of the spectra, followed by a transition to broad absorptions above 37,000 $cm^{-1}$. The *p*-methyl PPN's origin peak is at the highest energy of the three, and the closest one to the parent molecule. The higher resolution spectra of each molecule will be presented individually.

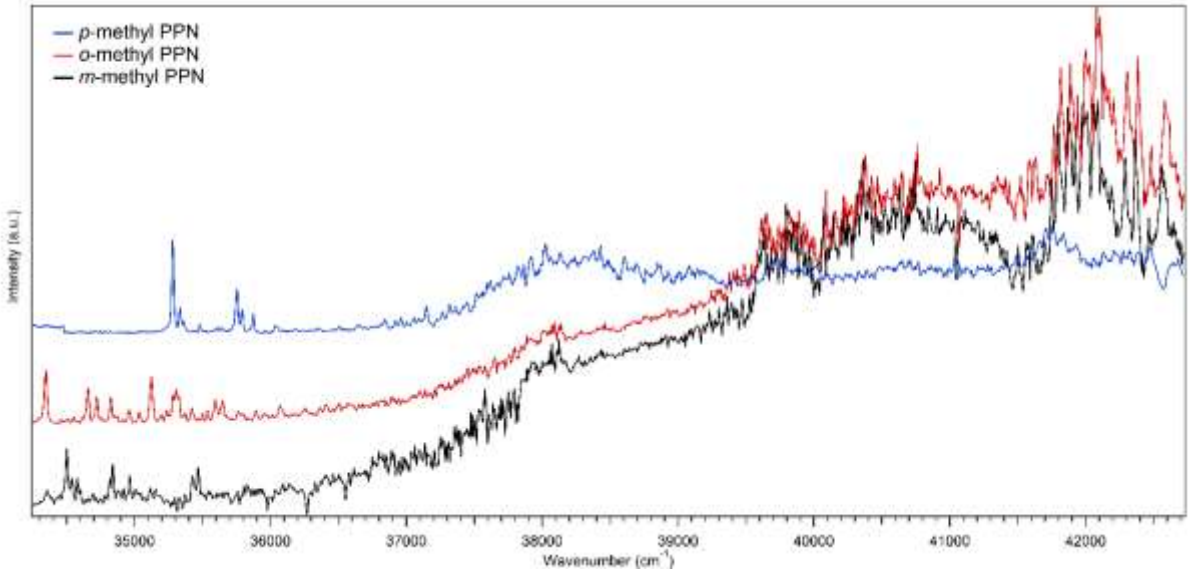


Figure 4.3 1C-R2PI overview scans of the *p*- (blue), *o*- (red), and *m*-methyl PPN (black).

### 4.3.1 *m*-methyl PPN

The UV spectrum of *m*-methyl PPN over the region of 34,200 to 36,360 $cm^{-1}$ is shown in Figure 4.4. The spectrum was recorded using both 2C-R2PI and LIF. The first peak, typically labeled the $S_0$-$S_1$ origin, is seen at 34,492 $cm^{-1}$, followed by a more intense peak just +3 $cm^{-1}$ above it. As will be explained in the discussion, the actual origin is the "+3" $cm^{-1}$ peak. Unusual Franck-Condon activity appears at +38, +77, and +97 $cm^{-1}$. As will be seen later, these low-frequency transitions are due to the methyl rotor, which must undergo a change in preferred orientation upon electronic excitation. Three more groupings of vibronic transitions at +318/321, +335/338, and

+461/464 $cm^{-1}$ serve as starting points for similar methyl rotor activity. Finally, transitions at +804, +926, and +965 $cm^{-1}$ are also likely vibronic fundamentals, since they have similar methyl rotor patterns built off them.

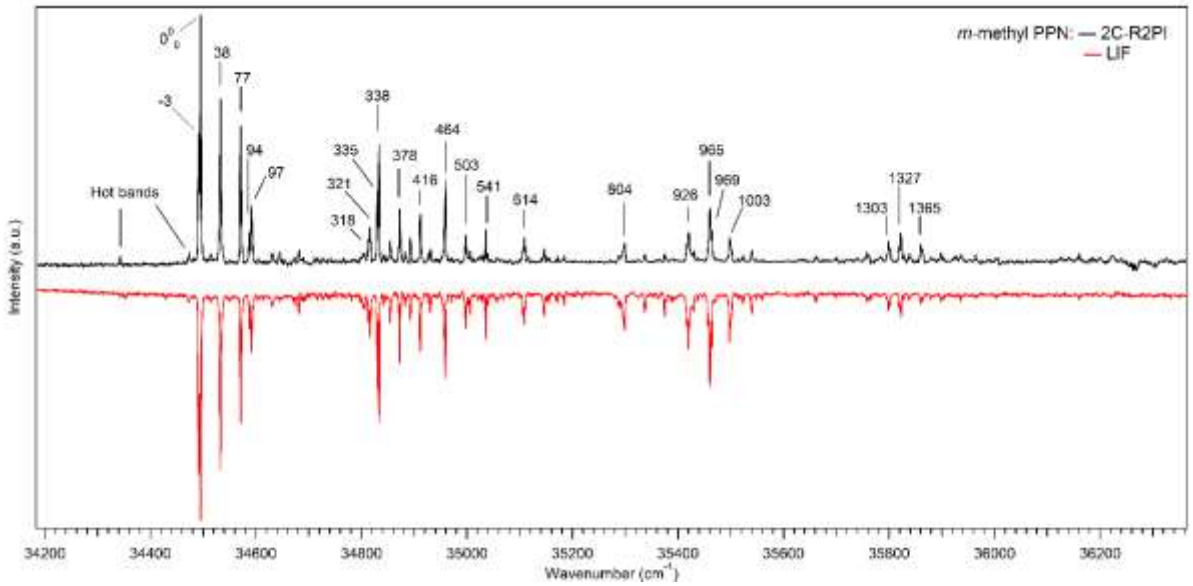


Figure 4.4 2C-R2PI (black), LIF (red).

PIE scans using both the origin and the -3 $cm^{-1}$ peaks as intermediate states are shown in Figure 4.5. Not surprisingly, given the presence of rather strong methyl rotor vibronic activity, the initial onset of ionization – which gives the adiabatic ionization potential – also shows steps at

thresholds related to the higher methyl rotor transitions. Nevertheless, the onset of first ion signal appears for both transitions near 38,674 ± 41 $cm^{-1}$.

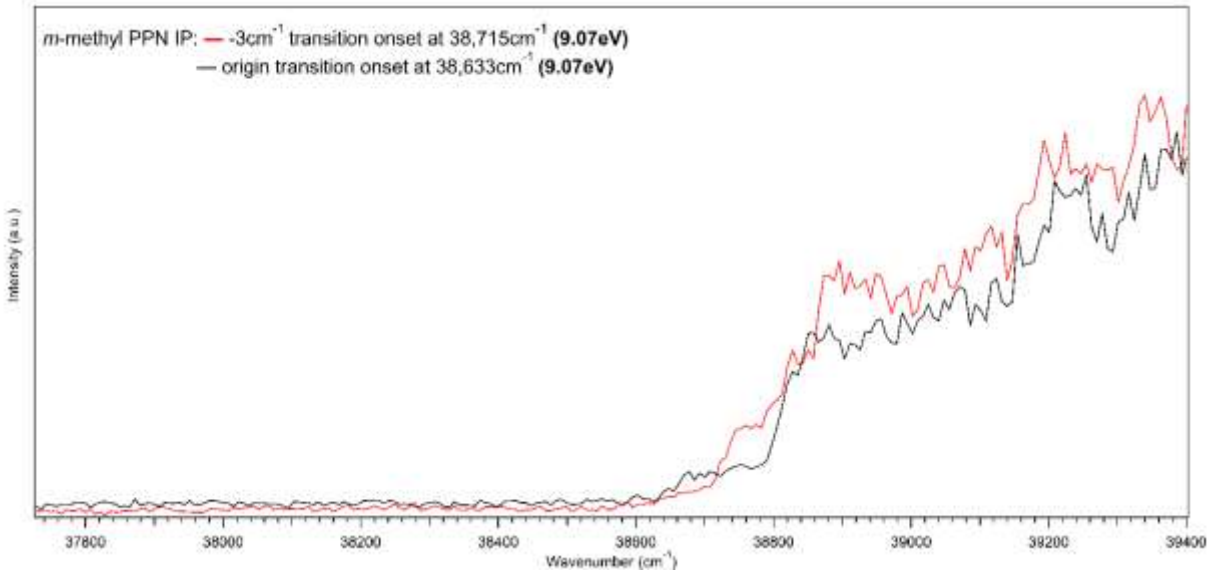


Figure 4.5 Ionization potentials of both the -3 $cm^{-1}$ (red) and the origin peak (black) of *m*-methyl PPN. Ionization onset of the -3 $cm^{-1}$ peak is appropriately shifted relative to the origin to account for the difference in energy between the two.

As the fluorescence was very low for all three molecules, including the *m*-methyl PPN, we were able to record DF spectra for only the origin and the strong transitions anticipated to be due to the methyl rotor (Fig. 4.6). However, information may still be gleaned from them that enables us to characterize the methyl rotor barriers and orientational preferences. Each DF spectrum shows

a peak very close to the resonant fluorescence that will enable us to identify the ground state rovibrational levels due to the rotation of the methyl group.

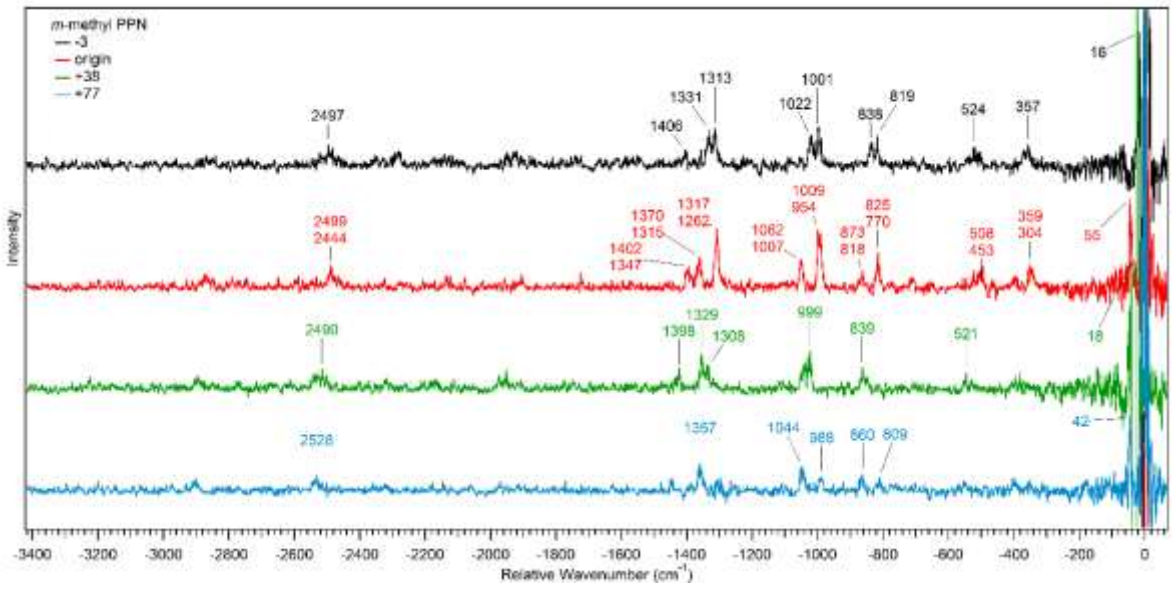


Figure 4.6 *m*-methyl PPN DF spectra on the origin, -3, +38, and +77 $cm^{-1}$ transitions. The second number listed for each peak in the origin trace represents the difference in wavenumber between that peak and the +55 $cm^{-1}$ peak.

### 4.3.2 *o*-methyl PPN

The *o*-methyl PPN excitation spectra are shown in Figure 4.7. Unlike the last molecule, this one's excitation spectra more closely resemble PPN in that there isn't much – if any – Franck-Condon activity in the low-frequency region where methyl rotor transitions would be anticipated. This likely means that there is no change in preferred orientation of the methyl group between ground and excited state, a point to which we will return in the discussion section.

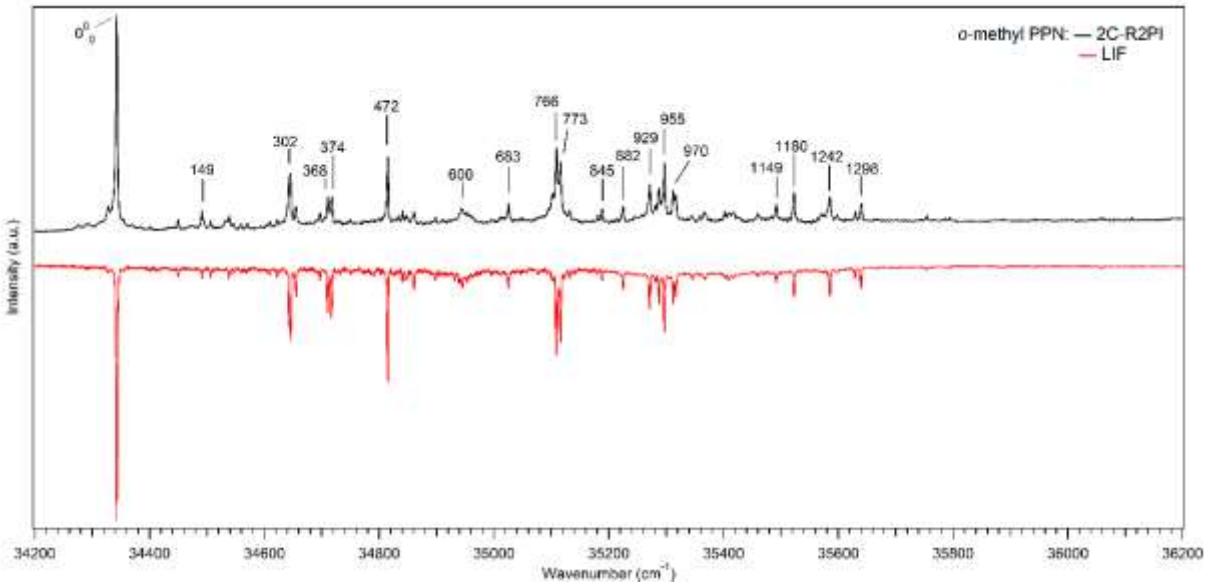


Figure 4.7 2C-R2PI (black), LIF (red).

The ionization potential (Fig. 4.8) is quite close to the *m*-methyl PPN at 9.05 eV, with just as sharp an onset, which strongly suggests that the geometries of the excited state and the ion must be very similar.

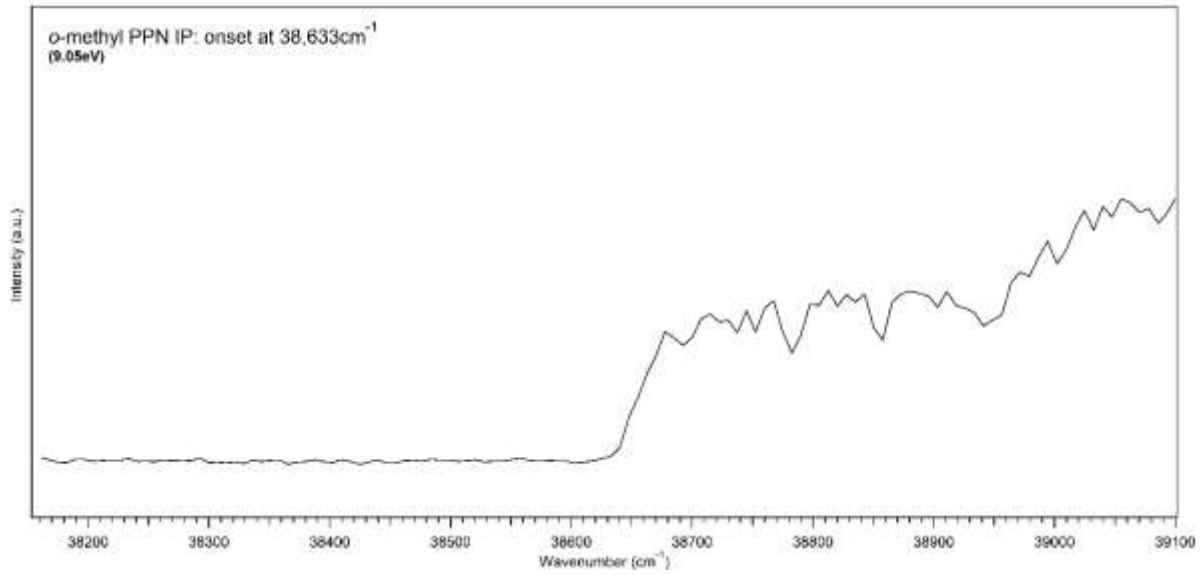


Figure 4.8 Ionization potential of *o*-methyl PPN. Sharp onset is seen at 38,633 cm$^{-1}$.

The DF in this case was better than either of the other two methylated PPN molecules (Fig. 4.9), and it was quite different from the excitation spectra, suggesting the ground state potential energy surface looks quite different to that of the excited state. Interestingly, we see a repetition of the +356/379 $cm^{-1}$ pair of peaks from PPN: in this case, the first is shifted to much lower frequency at +302, while the second is nearer at +374 $cm^{-1}$. And, just as before, one is an in-plane vibrational mode (a'), and the second is an out-of-plane mode (a"), though the order is reversed. Higher up are the two most intense peaks, +787 and 1295 $cm^{-1}$, which are totally symmetric fundamentals. The +787 $cm^{-1}$ mode closely resembles the 7a mode in benzene.

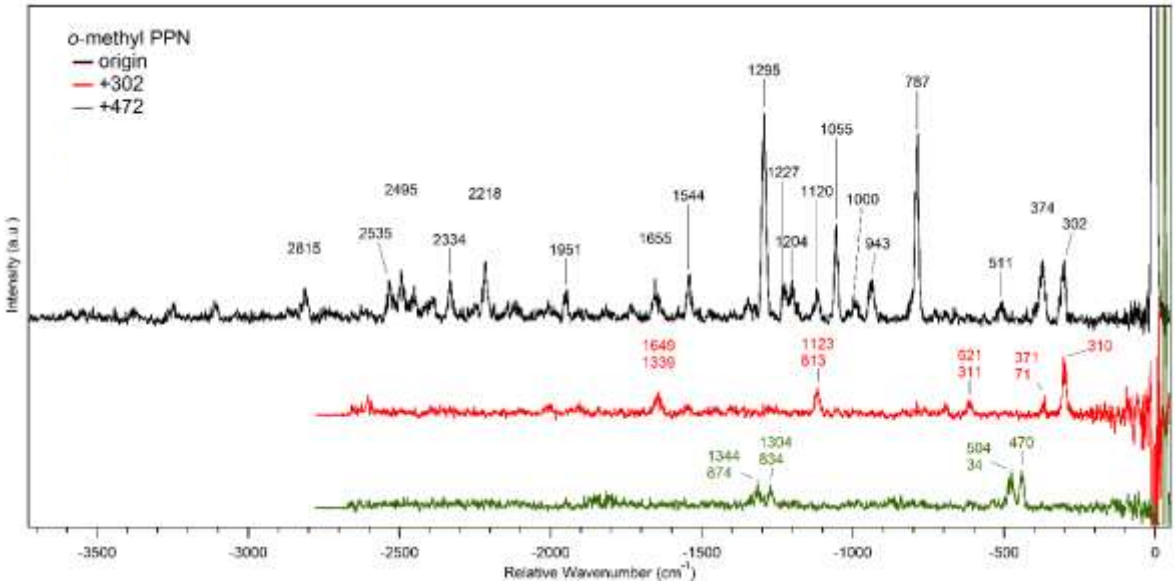


Figure 4.9 *o*-methyl PPN DF spectra of the origin, +302, and +472 $cm^{-1}$ transitions.

### 4.3.3 *p*-methyl PPN

The R2PI is shown alongside LIF in Figure 4.10. Note that the drop-off in fluorescence is seen quite quickly, at approximately 35,900 $cm^{-1}$, while the spectrum seems to continue in the R2PI. This is likely due to some non-radiative processes becoming dominant at that point. Also note that the R2PI does not continue past 36,300 $cm^{-1}$ due to limits with laser power and ion signal

intensity. In these spectra we see some signs of methyl rotor activity in the presence of the +18, +52 $cm^{-1}$, and the shoulders of some of the larger peaks (such as the +450 $cm^{-1}$ peak).

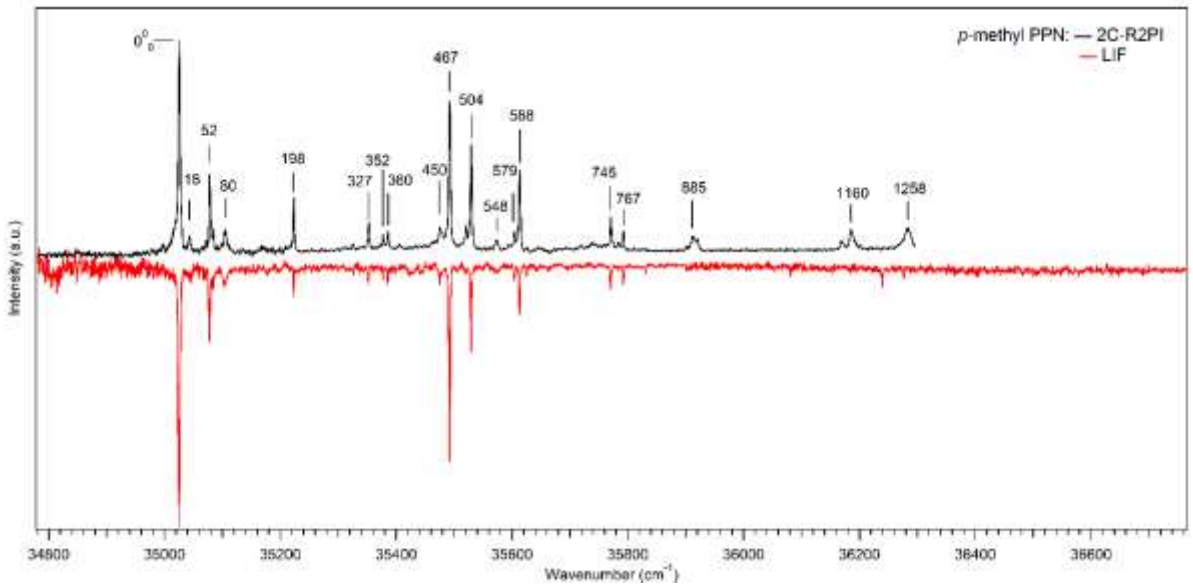


Figure 4.10 2C-R2PI (black), LIF (red).

The ionization potential (Fig. 4.11) of *p*-methyl PPN was sharp, as the others were, but was the smallest of the set, at 8.93 eV. The sharpness of the transition once again strongly indicates the geometries of both excited state and ion are similar.

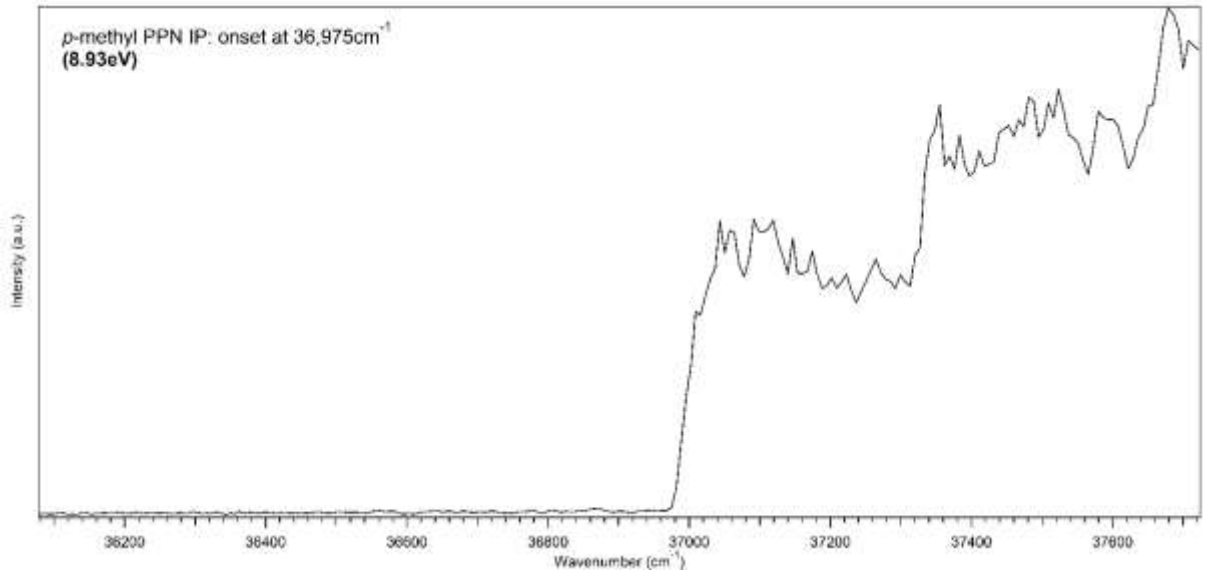


Figure 4.11 Ionization potential of *p*-methyl PPN. Sharp onset is seen at 36,975 cm$^{-1}$.

The *p*-methyl PPN DF (Fig. 4.12) could only be collected on the origin and the +467 cm$^{-1}$ peak. In this case, we can say that neither DF spectrum is a mirror image of the excitation spectrum, thus suggesting the ground and excited state have different geometries. All but the first peak of the

origin DF can be assigned to totally symmetric fundamentals, with the +465 $cm^{-1}$ resembling benzene's 16b mode.

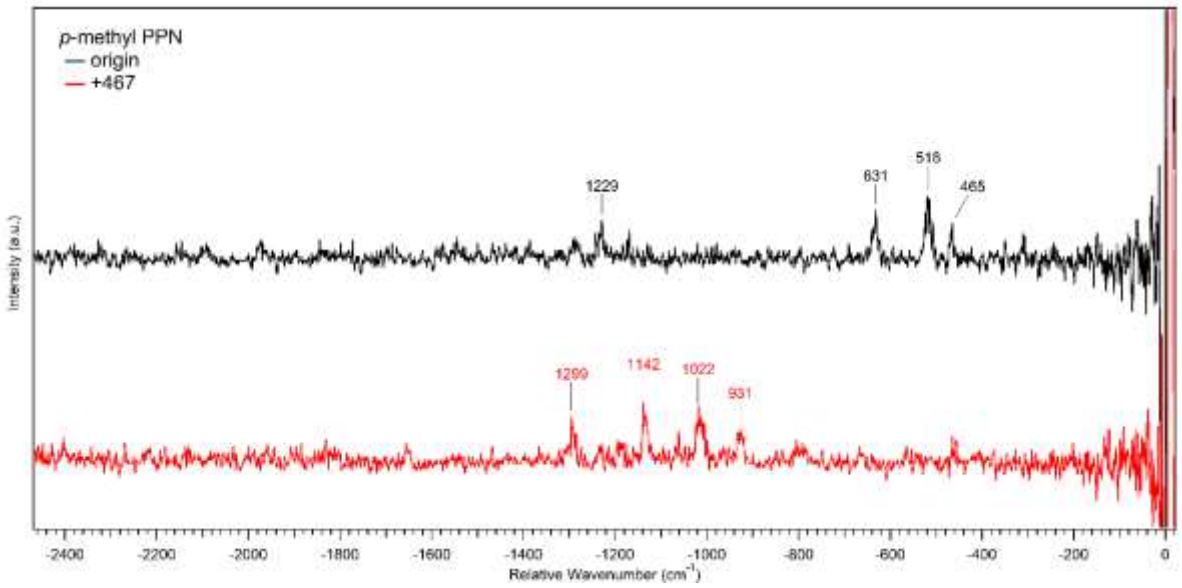


Figure 4.12 *p*-methyl PPN DF spectra of the origin and +467 $cm^{-1}$ transitions.

## 4.4 Discussion

All methylated versions of 3-phenyl-2-propynenitrile had very short-lived excited state lifetimes: on the order of the laser pulse, at <10 ns, in both R2PI and fluorescence. While this aspect of their lifetime matched that of the parent molecule, none of them showed a long-lived component that PPN had. 1C- and 2C-R2PI were both easily obtained, allowing us to get accurate measurements of the ionization potentials of each molecule (Table 4.2). These values are quite typical for benzene-like π-π* transitions.

Table 4.2 Summary of ionization potentials for all four molecules

| | Experiment (eV) | Calculation (eV) |
|---|---|---|
| PPN | -- | 8.85 |
| *o*-methyl PPN | 9.05 | 8.80 |
| *m*-methyl PPN | 9.07 | 8.82 |
| *p*-methyl PPN | 8.93 | 8.68 |

The origins of all three molecules were within the range expected: the *p*-methyl PPN was the closest to that of PPN at 35,025 $cm^{-1}$, with *o*- and *m*-methyl PPN at 34,343 $cm^{-1}$ and 34,495 $cm^{-1}$, respectfully. A direct comparison of all four molecules' excitation spectra is shown in Figure 4.13. In all cases, the origin peak is the strongest peak, and activity is generally present in clumps at about +450 $cm^{-1}$ and +980 $cm^{-1}$.

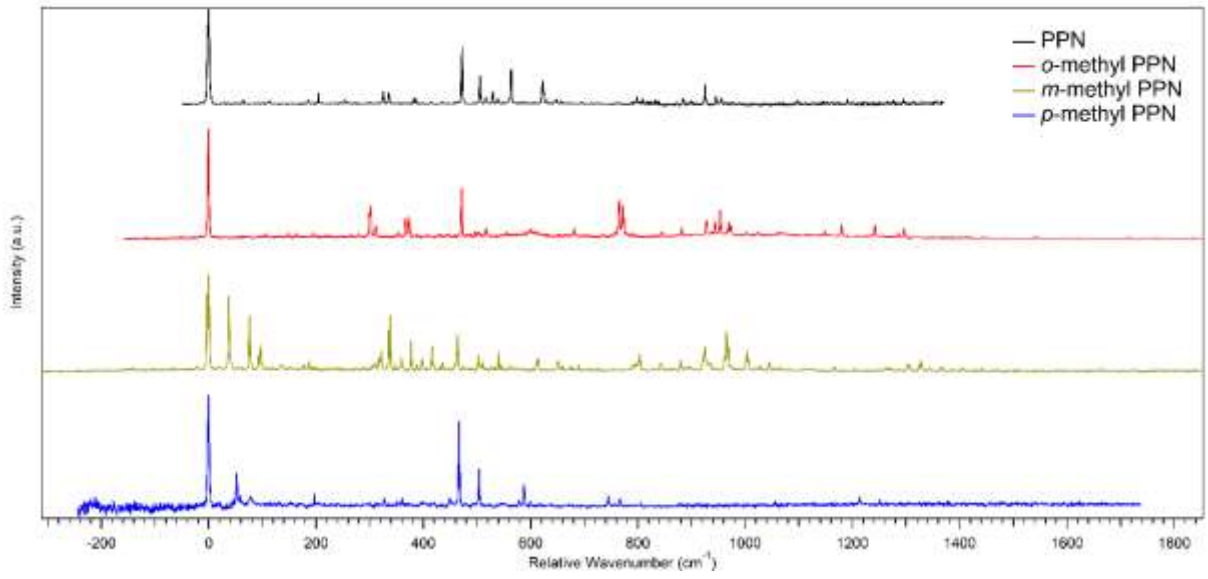


Figure 4.13 The LIF of the parent molecule PPN (black) with the *o*-, *m*-, and *p*-methyl PPN shown in red, gold, and blue respectively. All spectra have been shifted such that the origins of each begins at 0 $cm^{-1}$.

Fluorescence quantum yield was very small, yielding low signal-to-noise ratios in dispersed fluorescence and making it difficult to map out the $S_0$ state for all the methyl PPN molecules.

Methyl-rotor activity is most strongly seen in the *m*-methyl PPN. The strong Franck-Condon activity in the methyl rotor transitions indicates a change in the orientation of the methyl group relative to the benzene ring upon electronic excitation. As has been done before with similar meta-substituted toluenes (such as the *m*-chloro- and *m*-fluorotoluene[3-4]), the three-fold symmetry of the methyl torsional levels is treated within the $G_6$ molecular symmetry group, which is equivalent to the $C_{3v}$ point group.[5] This sets the symmetry levels of the torsional states as either $a_1$, $a_2$, or *e*. Figure 4.14 illustrates the energy levels involved in the *m*-methyl PPN, using the LIF excitation spectrum to map out the excited state levels and DF to derive the ground state levels. A powerful aspect of the DF spectra is that emission from an 'a' torsional level will be exclusively to 'a' levels in the ground state. The $0^0_0$ ($0a_1$-$0a_1$) band is associated with the most intense peak of the excitation spectra, and is taken as '0' relative wavenumbers, making the other, smaller peak at -3 $cm^{-1}$ the 1e"-1e' transition. The internal rotation F associated with the methyl group bound to a phenyl ring is about 5.4 $cm^{-1}$. If the molecule had no barrier to internal rotation, so that it rotated freely, the internal rotor levels would have values of

$$E_{int.\,rot.} = F \cdot m^2 \text{ where } m=0, \pm1, \pm2, \ldots$$

so that $0a_1$, 1e, 2e, $3a_2/3a_1$ would be at 0, 5.4, 22, and 49 $cm^{-1}$, respectively. Since these are values close to the ground state values deduced from the DF spectra, they indicate that the ground state 3-fold barrier is very low, probably $V_3 < 10$ $cm^{-1}$. In the excited state, the internal rotor levels show a smaller splitting between $0a_1$' and 1e' (~1 $cm^{-1}$), and larger 1e'↔2e' splitting of 44 cm-1, indicating that the excited state internal rotor barrier will be larger. Comparing these levels with

those in *m*-chloro[3] and *m*-fluorotoluene,[4, 6] we estimate an excited state barrier of $V_3$' near 100 $cm^{-1}$ in $S_1$ for *m*-methyl PPN, much as it is in those molecules.

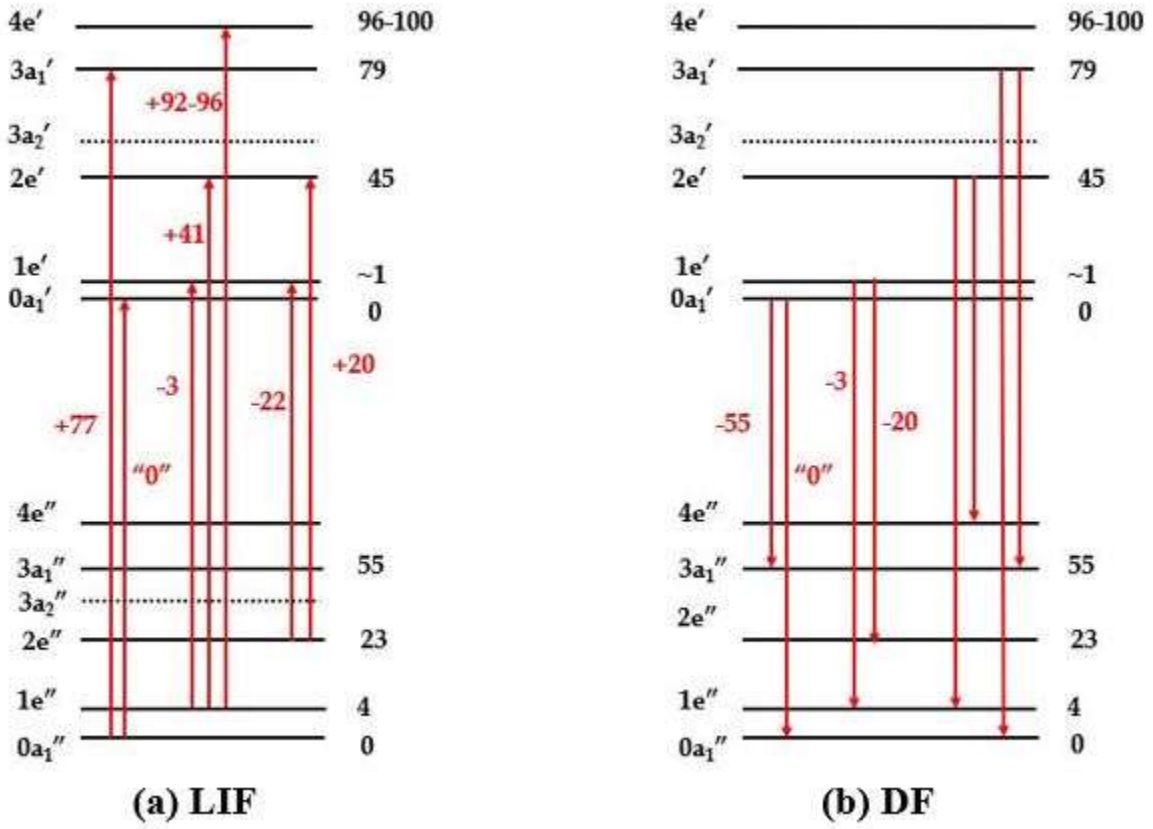


Figure 4.14 Schematic of the methyl torsional levels in *m*-methyl PPN, with LIF representing the excited state levels and DF representing the ground state levels. Arrows indicate the transitions and the values in red are the associated differences in wavenumber.

## 4.5 Conclusion

While more work is needed to understand the spectroscopy, including methyl-rotor calculations, we can make a generalized case for the *m*-methyl PPN. In treating it as though it has $C_{3v}$ symmetry, we can make assignments in the spectrum as either *a* or *e* symmetry transitions. In this way we have identified the origin as the +3 $cm^{-1}$ peak rather than the first peak seen in the spectrum and identified various transitions as belonging to *a-a* or *e-e* transitions. We have also in this way estimated the $V_3$ barrier height to be 10 $cm^{-1}$ and 100 $cm^{-1}$ in $S_0$ and $S_1$ respectively. The

*o*-methyl PPN had very little methyl rotor activity, which is consistent with other *o*-substituted toluenes.

All molecules shared similarities with PPN in their excited state spectra: they all had a doublet between 300-400 $cm^{-1}$, followed by a large peak at +470 $cm^{-1}$, and a group of peaks near 980 $cm^{-1}$. As many of these peaks were associated with either $b_1$ or $b_2$ vibrational fundamentals in PPN, and we know in that case that vibronic coupling is responsible for much of it, we can definitively state that vibronic coupling must also play a significant role in the methylated PPN spectra.

## 4.6 References

1. Luo, F.-T., et. al., Org. Syntheses, 1998. **75**: p. 146-151.

2. Gaussian 09, R.B., D.01, M. J. Frisch, G. W. Trucks, H. B. Schlegel, G. E. Scuseria, M. A. Robb, J. R. Cheeseman, G. Scalmani, V. Barone, B. Mennucci, G. A. Petersson, H. Nakatsuji, M. Caricato, X. Li, H. P. Hratchian, A. F. Izmaylov, J. Bloino, G. Zheng, J. L. Sonnenberg, M. Hada, M. Ehara, K. Toyota, R. Fukuda, J. Hasegawa, M. Ishida, T. Nakajima, Y. Honda, O. Kitao, H. Nakai, T. Vreven, J. A. Montgomery, Jr., J. E. Peralta, F. Ogliaro, M. Bearpark, J. J. Heyd, E. Brothers, K. N. Kudin, V. N. Staroverov, T. Keith, R. Kobayashi, J. Normand, K. Raghavachari, A. Rendell, J. C. Burant, S. S. Iyengar, J. Tomasi, M. Cossi, N. Rega, J. M. Millam, M. Klene, J. E. Knox, J. B. Cross, V. Bakken, C. Adamo, J. Jaramillo, R. Gomperts, R. E. Stratmann, O. Yazyev, A. J. Austin, R. Cammi, C. Pomelli, J. W. Ochterski, R. L. Martin, K. Morokuma, V. G. Zakrzewski, G. A. Voth, P. Salvador, J. J. Dannenberg, S. Dapprich, A. D. Daniels, O. Farkas, J. B. Foresman, J. V. Ortiz, J. Cioslowski, and D. J. Fox, Gaussian, Inc., Wallingford CT, 2010, 2013.

3. Feldgus, S.H., et. al., Int. J. Mass Spectrom. Ion Process., 1996. **159**: p. 231-244.

4. Takazawa, K., et. al., J. Chem. Phys., 1993. **99**: p. 3205-3217.

5. Bunker, P.M., Molecular Symmetry and Spectroscopy. Academy Press, New York. 1979.

6. Rudolph, H., and A. Trinkaus, Z. Naturforsch. A, 1968. **23A**: p. 68.

# PUBLICATION

THE JOURNAL OF PHYSICAL CHEMISTRY A

Article

pubs.acs.org/JPCA

## Rate Constant and Mechanism of the Reaction Cl + $CFCl_2H$ → $CFCl_2$ + HCl over the Temperature Range 298−670 K in $N_2$ or $N_2/O_2$ Diluent

E. W. Kaiser[†,*] and Khadija M. Jawad[†,‡]

[†]Department of Natural Sciences, University of Michigan—Dearborn, 4901 Evergreen Road, Dearborn, Michigan 48128, United States

[‡]Department of Chemistry, Purdue University, West Lafayette, Indiana 47907, United States

**ABSTRACT:** The rate constant of the reaction Cl + $CFCl_2H$ ($k_1$) has been measured relative to the established rate constant for the reaction Cl + $CH_4$ ($k_2$) at 760 Torr. The measurements were carried out in Pyrex reactors using a mixture of $CFCl_2H$, $CH_4$, and $Cl_2$ in either $N_2$ or $N_2/O_2$ diluent. Reactants and products were quantified by GC/FID analysis. Cl atoms were generated by irradiation of the mixture with 360 nm light to dissociate the $Cl_2$ for temperatures up to ~550 K. At higher temperature, the $Cl_2$ dissociated thermally, and no irradiation was used. Over the temperature range 298−670 K, $k_1$ is consistently a factor of ~5 smaller than that of $k_2$ with a nearly identical temperature dependence. The optimum non-Arrhenius rate constant is represented by the expression $k_1 = 1.14 \times 10^{-22}\, T^{3.49}\, e^{-241/T}$ cm$^3$ molecule$^{-1}$ s$^{-1}$ with an estimated uncertainty of ±15% including uncertainty in the reference reaction. $CFCl_3$ formed from the reaction $CFCl_2$ + $Cl_2$ ($k_3$) is the sole product in $N_2$ diluent. In ~20% $O_2$ at 298 K, the $CFCl_3$ product is suppressed. The rate constant of reaction 3 was measured relative to that of reaction 4 [$CFCl_2$ + $O_2$ ($k_4$)] giving the result $k_3/k_4 = 0.0031 \pm 0.0005$ at 298 K. An earlier experiment by others observed C(O)FCl to be the major product of reaction channel 4 [formed via the sequence, $CFCl_2(O_2) \rightarrow CFCl_2O \rightarrow C(O)FCl + Cl$]. Our current experiments verified that there is a Cl atom chain reaction in the presence of $O_2$ as required by this mechanism.

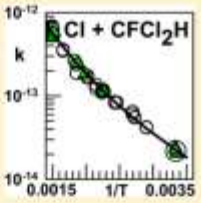




### 1. INTRODUCTION

The relative rate method is a powerful technique for measuring rate constants of reactions, and it has been used extensively in the studies of Cl atom reactions with organic molecules. To use it effectively, well-known rate constants for reference reactions are needed, particularly as a function of temperature. There are a few well-documented reference reactions whose rate constants have been carefully studied over a wide temperature range, in particular Cl + $CH_4$[1] and Cl + $C_2H_6$.[2] References 1 and 2 compare several sets of data over temperature ranges of 200−1100 and 200−1000 K for methane and ethane, respectively. However, for slower Cl reactions with organic molecules (rate constants of the order of $10^{-14}$ cm$^3$ molecule$^{-1}$ s$^{-1}$ at ambient temperature), comprehensive data are sparse. The most extensive temperature-dependent studies of which we are aware have been performed on $CFCl_2H$ (298−433 K) and $CF_2ClH$ (296−411 K)[3] and on $CF_3CFH_2$ (298−423 K).[4] Because of the importance of having well established reference reactions over a wide range of temperature, we have undertaken a relative rate measurement of the rate constant of reaction 1

$$Cl + CFCl_2H \rightarrow CFCl_2 + HCl \quad (1)$$

$$Cl + CH_4 \rightarrow CH_3 + HCl \quad (2)$$

over the temperature range 298−670 K using reaction 2 as the reference. In addition, the ratio of the rate constant for the reaction of the free radical product $CFCl_2$ with $Cl_2$ relative to its reaction with $O_2$ ($k_3/k_4$) was determined at ambient temperature

$$CFCl_2 + Cl_2 \rightarrow CFCl_3 + Cl \quad (3)$$

$$CFCl_2 + O_2 \rightarrow CFCl_2O_2 \quad (4)$$

Subsequent reactions of $CFCl_2O_2$ have been observed to yield chlorofluoroformaldehyde, C(O)FCl, in high yield at ambient temperature,[5] and the effect of this free radical channel on reaction 1 has also been examined at 298 K.

### 2. EXPERIMENTAL SECTION

The GC/FID (HP 5890) temperature program and column have been described in detail previously.[6] In the current GC/FID experiments, a spherical (500 cm$^3$) Pyrex reactor was used for ambient-temperature measurements. The experiments were performed using initial mixtures of $Cl_2$ (99.7%), $CFCl_2H$ (Synquest Laboratories, 98%), and a kinetic reference compound in $N_2$ (99.999% min) or $N_2/O_2$ (99.998%) diluent. In all experiments, $CH_4$ (99.99%) was added as the kinetic reference compound. In addition, $CF_2Cl_2$ (99%), which does not react with Cl, was included in the mixture for internal calibration of the GC samples. Freeze/thaw degassing cycles were performed on all condensable reactants.

Chlorine atoms were generated by irradiation of the unreacted mixture with UV light peaking near 360 nm using a single Sylvania F6T5 BLB fluorescent lamp. To verify that radiation inhomogeneity from the single lamp did not affect the results, an experiment was performed at ambient temperature in the 500 cm$^3$ reactor using two lamps placed on opposite sides of the reactor. As expected, the reaction proceeded twice

Received: February 26, 2014
Revised: April 14, 2014
Published: April 15, 2014

   dx.doi.org/10.1021/jp502023f | J. Phys. Chem. A 2014, 118, 3237−3242

Table 1. Initial Conditions, Product Yields, and $k_1/k_2$ for Selected Data Points

| | T (K) | irradiation time (sec) | $[C]/[C]_0$ ($CH_4$)[a] | $\Sigma CH_xCl_{4-x}$ yield (%) | $[C]/[C]_0$ ($CFCl_2H$)[a] | $CFCl_3$ yield (%) | $k_1/k_2$ | $[Cl_2]_0$ (ppm) | $[O_2]_0$ (ppm) |
|---|---|---|---|---|---|---|---|---|---|
| 1 | 298 | 120 | 0.347 | 95 ± 10 | 0.812 | 91 ± 10 | 0.197 | 1100 | 0 |
| 2 | 298 | 460 | 0.598 | 2 ± 1 | 0.906 | <5 | 0.192 | 1020 | 182 000 |
| 3 | 495 | 40 | 0.313 | 108 ± 10 | 0.798 | 99 ± 10 | 0.194 | 1060 | 0 |
| 4 | 495 | 120 | 0.06 | 107 ± 10 | 0.56 | 104 ± 10 | 0.205 | 1060 | 0 |
| 5 | 504 | 1920 | 0.34 | 2.5 ± 1 | 0.804 | 15 ± 2 | 0.202 | 2450 | 200 000 |
| 6 | 534 | 1800 | 0.179 | 12 ± 1 | 0.696 | 67 ± 7 | 0.211 | 2450 | 206 000 |
| 7 | 534 | 960 (n.i.)[b] | 0.999 | | 1.003 | | | 2450 | 200 600 |
| 8 | 539 | 30 | 0.469 | 108 ± 10 | 0.855 | 102 ± 10 | 0.206 | 1000 | 0 |
| 9 | 539 | (n.i.)[c] | 0.904 | | 0.992 | | | 1000 | 0 |
| 10 | 605 | 15 | 0.239 | 108 ± 10 | 0.746 | 106 ± 10 | 0.200 | 980 | 0 |
| 11 | 605 | (n.i.) | 0.407 | 112 ± 10 | 0.836 | 104 ± 10 | 0.200 | 980 | 0 |
| 12 | 660 | (n.i.) | 0.384 | 107 ± 10 | 0.812 | 100 ± 10 | 0.221 | 303 | 0 |
| 13 | 670 | (n.i.) | 0.074 | 109 ± 10 | 0.496 | 104 ± 10 | 0.269 | 840 | 0 |
| 14 | 669 | 120 (n.i.) | 0.202 | 50 ± 5 | 0.712 | 85 ± 9 | 0.212 | 423 | 205 000 |

[a]Fractional consumption of $CH_4$ and $CFCl_2H$. [b]960 (n.i.) = placed in the reactor for 960 s with no irradiation. [c](n.i.) = in the reactor for the minimum time (~45 s) necessary to fill the reactor and sample with irradiation off.

as fast, but no change in the rate constant ratio or the product yields was observed. After a chosen irradiation time, a portion of the contents of the reactor was removed into a 2.5 $cm^3$ gastight syringe (Hamilton Co.) and analyzed by injection of 1 $cm^3$ of this sample into the injector port (at 373 K) of the gas chromatograph. The presence of the internal calibration species, $CF_2Cl_2$, permitted corrections to be made for uncertainty in the precise amount of sample injected into the GC using the syringe. The mixture in the 500 $cm^3$ reactor was then irradiated for additional times, and additional analyses were performed. All ambient temperature experiments in this reactor were carried out at a total pressure of 800−950 Torr. The reactant mole fraction ranges for the measurement of $k_1$ were $Cl_2$ (290−3100 ppm); $CFCl_2H$ (120−370 ppm); $CH_4$ (60−220 ppm); $CF_2Cl_2$ (45 ppm); and $O_2$, when present (180−220 Torr); balance $N_2$.

Elevated temperature experiments were performed over the range 298−670 K using a 40 $cm^3$, cylindrical, Pyrex reactor (26 mm ID × ~7 cm length) with a thermocouple well along the axis and a Teflon-sealed, glass stopcock attached to a Pyrex capillary tube at the end opposite the thermocouple well. This reactor was placed inside a tube oven, whose lid remained open approximately 6 mm to allow radiation from the fluorescent lamp to enter. The calibration of the chromel−alumel thermocouple was checked in ice, boiling water, and hot oil (570 K), whose temperature was measured by a calibrated thermometer. The temperature along the axis of the reactor was uniform to ±0.5% from the mean. The temperature calibration was also verified at ~715 K using a volumetric expansion method. A known pressure of $N_2$ was placed into the hot reactor and then was expanded into a similar known volume at ambient temperature. From these data, the average temperature of the reactor was calculated to be 705 K, while the average thermocouple temperature along the axis of the reactor was measured to be 717 K. The agreement is within the experimental error of this technique.

During a high temperature experiment, a portion of the unreacted mixture was placed into the reactor at pressures varying from 650 to 760 Torr depending on the depletion in the reactant storage flask. The mixture was then irradiated for a chosen time, and a portion of the contents were withdrawn into the gastight syringe. Only one irradiation was possible per sample placed into this reactor because of the large sample loss during the sampling procedure.

$CH_4$, $CF_2Cl_2$, and $CFCl_2H$ were also placed individually in the high temperature reactor in the absence of $Cl_2$ without irradiation to determine the degree of thermal decomposition that may occur as the temperature is increased. No thermal decomposition was observed for any of these species at temperatures up to 670 K. Thermal decomposition of $CFCl_2H$ began at approximately 730 K, which is above the maximum temperature in these kinetics studies.

Identification and calibration of the reactants and products were carried out by injecting a known concentration of a pure species into the GC in the presence of an internal calibration species. This provides a determination of the FID sensitivity and the retention time for all of the compounds. Pure samples of $CH_4$, $CFCl_2H$, $CF_2Cl_2$, and $CFCl_3$ were used for identification and calibration. Pure samples of the methane primary product ($CH_3Cl$) and secondary products ($CH_2Cl_2$, $CHCl_3$, and $CCl_4$) were also available for calibration.

**2.1. Sample Stability in the Sampling Syringe.** To explore a possible perturbation of samples by the gastight syringe, a test irradiation was run in the 500 $cm^3$ reactor at ambient temperature in a mixture of $Cl_2$ (3500 ppm), $CH_4$ (94 ppm), $CFCl_2H$ (91 ppm), and $CF_2Cl_2$ (225 ppm). No $O_2$ was added. Thirty-three percent of the $CFCl_2H$ and 85% of the $CH_4$ were consumed. The first sample from this irradiation was withdrawn into the syringe and injected into the GC within ~30 s as is typical. A second sample from the same irradiated mixture was taken and allowed to sit for 14 min in the syringe before injection into the GC. No change was observed in the reactant consumption or product yields in this second analysis to within experimental error. This confirms that no measurable loss occurs in the syringe.

## 3. RESULTS AND DISCUSSION

**3.1. Rate Constant of Reaction 1.** Table 1 presents selected data points illustrating the types of experiments performed and representative results obtained. Examples are included covering the full temperature range studied, as well as the $Cl_2$ and $O_2$ mole fraction ranges used. The data in Table 1 include the irradiation time, the fractional consumption of $CH_4$ and of $CFCl_2H$, the percentage yield of the chlorinated



dx.doi.org/10.1021/jp5020231 | J. Phys. Chem. A 2014, 118, 3237−3242

products, the rate constant ratio, and the initial $O_2$ and $Cl_2$ mole fractions.

Data points (DP) 1 and 2 at 298 K in Table 1 show that the rate constant ratio $k_1/k_2$ is not affected by the addition of 18% $O_2$ to the mixture. In the absence of $O_2$, the yields of chlorinated products from methane ($\Sigma_{x=0-3}$ $CH_xCl_{4-x}$) and $CFCl_2H$ ($CFCl_3$) after H atom abstraction are 100% to within the experimental error of ±10% of the measured yield. The addition of 18% $O_2$ suppresses the formation of $CFCl_3$ and reduces the chlorinated product yield from methane to near zero.

At 495 K (DP 3 and 4), the chlorinated product yields from both $CH_4$ and $CFCl_2H$ remain at 100% in the absence of $O_2$. The ratio $k_1/k_2$ is identical to that at 298 K to within experimental error. Thus, the temperature dependence of $k_1$ ($Cl + CFCl_2H$) is identical to that of $k_2$ ($Cl + CH_4$) over the temperature range 298–495 K. The data also show that the results are unaffected by the extent of consumption of the reactants.

The addition of ~20% $O_2$ while doubling the mole fraction of $Cl_2$ in the reactant mixture at 504 K produces no change in the relative rate constant ratio (DP 5). However, a 15% yield of the product $CFCl_3$ is now observed. Increasing the temperature to 534 K while keeping the initial reactant mole fractions constant (DP 6) increases the yield of $CFCl_3$ to 67% and the sum of the $CH_4$ products to 12%. We believe the increase in the chlorinated product yields from both reactants results from the onset of significant thermal reversibility of the $O_2$ addition reactions at 534 K. This reversibility will increase the steady-state concentrations of the $CH_3$ and $CFCl_2$ radicals in the reacting mixture resulting in an increase in $CH_3Cl$ and $CFCl_3$ generation as observed. At 534 K, a mixture identical to that in DP 6 was placed in the reactor in the absence of irradiation (DP 7). Neither $CFCl_2H$ nor $CH_4$ was consumed to within experimental error, indicating that no measurable thermal reaction occurs at this temperature in the presence of $O_2$. Two experiments (DP 8 and 9) at 539 K, which had no oxygen added, were performed in the presence and absence of irradiation. DP 9 (no irradiation) shows the onset of a slow thermal reaction resulting in a 10% loss of $CH_4$. No measurable loss of $CFCl_2H$ is observed. Comparing DP 8 (with irradiation) to DP 9, it is evident that irradiation is the major source of Cl atom formation at and below this temperature in $N_2$.

At 605 K, a very different result is observed. DP 10 presents data from an experiment in which a mixture was placed in the high temperature reactor and irradiated for 15 s. In DP 11, a second sample of the same unreacted mixture was placed into the reactor for a similar period of time but without irradiation. Comparing these data points reveals that approximately 2/3 of the reaction occurs by a thermal process at this temperature. Further examination of these two data points shows that the relative rate constant ratio and the product yields are identical. This provides evidence that the thermal reaction is initiated by dissociation of $Cl_2$ followed by a Cl atom chain reaction identical to that observed during irradiation of lower temperature mixtures. In particular, the relative rate constant ratios are identical showing that at high temperature the reaction can be studied solely using thermal reaction.

At 660–670 K, the thermal reaction becomes dominant, and no irradiation was used to determine the rate constant ratio and product yields. At this temperature, the thermal reaction is too rapid to be controlled by adjusting the residence time in the reactor since the minimum residence time required to fill the reactor and take a sample (~45 s) results in complete depletion of the $Cl_2$ reactant in the mixture. Adjusting the initial $Cl_2$ mole fraction was the only way to vary the degree of reactant consumption. This is illustrated by DP 12 and 13 in which the lower $Cl_2$ mole fraction present in DP 12 produces less reactant consumption. Finally, DP 14 confirms that the addition of ~20% $O_2$ to the mixture does not affect the measured rate constant ratio significantly as was observed at lower temperatures.

In summary, the measurement of the rate constant ratio $k_1/k_2$ is independent of the initial mixture composition. Specifically, variation of the initial $Cl_2$ from 300 to 3100 ppm and the initial $O_2$ from 0 to $2 \times 10^5$ ppm does not affect the measured rate constant ratio even though the radical concentrations can change dramatically. These observations indicate that the chemistry of this reacting system is well understood, as required in the relative rate measurement of a rate constant.

Figure 1 presents an Arrhenius-type plot of all of the rate constant measurements for reaction 1. These rate constants

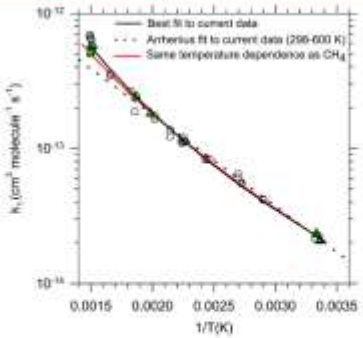


**Figure 1.** $Log_{10}$ of the rate constant of reaction 1 ($Cl + CFCl_2H$) plotted as a function of 1/T. Open circles are data obtained in $N_2$. Green filled triangles are data obtained in 20% $O_2$ with $N_2$ balance. The large circle at 298 K represents the average of 17 experiments at ambient temperature with the symbol size representing $2\sigma$ of the data scatter. The fits to the data are discussed in section 3.1. Arrhenius fit: $k_1 = 4.04 \times 10^{-12}\ e^{-1561/T}$. Same temperature dependence as $CH_4$ fit: $k_1 = 1.16 \times 10^{-19}\ T^{2.49}\ e^{-609/T}$. Best fit to current data: $k_1 = 1.14 \times 10^{-22}\ T^{3.44}\ e^{-241/T}$ $cm^3$ $molecule^{-1}$ $s^{-1}$.

were determined from the measured rate constant ratio $k_1/k_2$ using the rate constant expression $k_2 = 5.69 \times 10^{-19}\ T^{2.49}\ e^{-609/T}$ $cm^3$ $molecule^{-1}$ $s^{-1}$ determined by Bryukov et al.[1] The open circle data point at 298 K is an average of the 17 measurements at this temperature in the absence of $O_2$ with a $2\sigma$ error of ±10%. The other open circle symbols are individual determinations in the absence of $O_2$ whose precision is indicated by the data scatter. The green triangles were obtained from initial mixtures containing ~20% $O_2$.

Three fits to the data are shown. The dotted line represents an Arrhenius fit obtained over the temperature range 298–600 K ($k_1 = 4.04 \times 10^{-12}\ e^{-1561/T}$ $cm^3$ $molecule^{-1}$ $s^{-1}$). The red line represents a fit in which the temperature dependence of $k_1$ ($k_1 = 1.16 \times 10^{-19}\ T^{2.49}\ e^{-609/T}$ $cm^3$ $molecule^{-1}$ $s^{-1}$) is assumed to be identical to that of $CH_4$. This expression fits the data well except for a slightly faster increase in the experimentally measured $k_1$ at 660–670 K, although the data scatter increases



dx.doi.org/10.1021/jp502023f | J. Phys. Chem. A 2014, 118, 3237−3242

by a factor of ~1.05 at this temperature. The best fit to all of the data is shown by the blue line ($k_1 = 1.14 \times 10^{-22}\ T^{3.49}\ e^{-241/T}$ cm$^3$ molecule$^{-1}$ s$^{-1}$). Over the entire temperature range, the dependence of $k_1$ on $T$ remains very close to that of methane, while the pre-exponential factor decreases by a factor of ~5, close to the factor of 4 reduction in the number of hydrogen atoms in $CFCl_2H$.

Figure 2 presents a comparison of these three fits to previous measurements of $k_1$. The current measurements agree well with

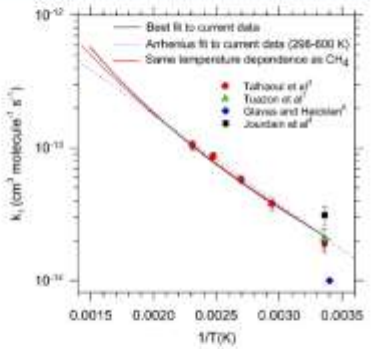


Figure 2. Comparison of the fits to the current data discussed in section 3.1 with previous measurements of $k_1$.

that of Tuazon et al.[7] at 298 K and with the temperature-dependent measurements of Talhaoui et al.[3] between 298 and 435 K. The measurements at 298 K by Glavas and Heicklen[8] and by Jourdain et al.[9] are in poorer agreement. We believe that the current measurements, corroborated by those of Talhaoui et al, who used an absolute rate method of measuring $k_1$ in the lower temperature range and by Tuazon et al. at ambient temperature, provide an accurate measurement of $k_1$ over the range 300–670 K. A discussion of the estimated error is presented in section 3.3.

**3.2. Determination of $k_3/k_4$.** The ratio of the rate constant for the reaction of the product radical from reaction 1 ($CFCl_2$) with $Cl_2$ ($k_3$) relative to that of its reaction with $O_2$ ($k_4$) was also measured at ambient temperature. As derived previously,[6] the ratio $k_3/k_4$ can be obtained from the expression

$$A = \{[Y(N_2)/Y(O_2)] - 1\}^{-1} = k_3/k_4\{[Cl_2]/[O_2]_{av}\}$$

In this expression, $Y(N_2)$ is the percentage yield of $CFCl_3$ in the absence of $O_2$ and $Y(O_2)$ is its yield in the presence of specified $[Cl_2]$ and $[O_2]_{av}$ mole fractions. The ratio $k_3/k_4$ is derived from the slope of a plot of $A$ vs $[Cl_2]/[O_2]_{av}$. The measured value of $Y(N_2)$ is 100% within experimental error at ambient temperature as shown in Table 1. A few selected data points from the determination of $k_3/k_4$ are shown in Table 2. This table presents the irradiation time, the fraction of $CFCl_2H$ consumed, the $CFCl_3$ yield, the value of $A$ calculated from this yield, the initial mole fractions of the reactants, and the average $O_2$ mole fraction ($[O_2]_{av}$) present during the reaction. Reaction 4 is followed by reactions 5 and 6.

$$CFCl_2O_2 + CFCl_2O_2 \rightarrow CFCl_2O + CFCl_2O + O_2 \quad (5)$$

$$CFCl_2O \rightarrow C(O)FCl + Cl \quad (6)$$

Because reaction 4 is much faster that reaction 3 (see below), a large initial concentration coupled with a substantial consumption of $CFCl_2H$ and a low concentration of $O_2$ must be used so that the $CFCl_3$ product is large enough to be measurable. This means that significant consumption of the initial $O_2$ may occur. Reactions 4–6 show that 1/2 of an $O_2$ is consumed for every $CFCl_2H$ that is consumed by reaction with $O_2$. Using this observation, the final $[O_2]_f$ mole fraction at the end of an irradiation can be estimated, and $[O_2]_{av} = \{[O_2]_0 + [O_2]_f\}/2$. This is the value used in the expression for $A$ above. A corresponding correction for $[Cl_2]$ is not required because the initial chlorine concentrations are much larger.

The ranges of initial composition of the reactants were $[O_2]$ = 108–352 ppm and $[Cl_2]$ = 830–6100 ppm. $CF_2Cl_2$ was again present as an internal calibrant. No $CH_4$ was added to these mixtures. The rate constant ratio determined from the slope of the line in Figure 3 is $k_3/k_4 = 0.0031 \pm 0.0005$. Thus, $CFCl_2$

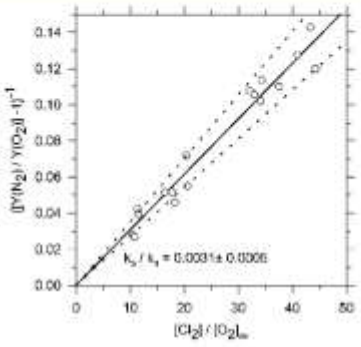


Figure 3. Determination of the rate constant ratio for the reaction of $CFCl_2$ with $Cl_2$ relative to the reaction of $CFCl_2$ with $O_2$. See the discussion in section 3.2.

reacts 322 times faster with $O_2$ than with $Cl_2$. A nearly identical result has been observed previously in a study of the reaction of the chlorofluoroalkyl radicals formed from the addition reaction

**Table 2. Initial Conditions and $CFCl_3$ Yield for Selected Data Points Used to Derive $k_3/k_4$**

| | irradiation time (sec) | $[C]/[C]_0$[a] ($CFCl_2H$) | $CFCl_3$ yield (%) | $A$[a] | $[CFCl_2H]_0$ (ppm) | $[Cl_2]_0$ (ppm) | $[O_2]_0$ (ppm) | $[O_2]_{av}$ (ppm) |
|---|---|---|---|---|---|---|---|---|
| 1 | 60 | 0.522 | 9.9 | 0.11 | 106 | 3275 | 100 | 87 |
| 2 | 30 | 0.544 | 9.7 | 0.107 | 93 | 6100 | 200 | 190 |
| 3 | 60 | 0.283 | 9.54 | 0.106 | 93 | 6100 | 200 | 185 |
| 4 | 120 | 0.039 | 9.25 | 0.102 | 93 | 6100 | 200 | 179 |
| 5 | 180 | 0.10 | 2.7 | 0.0277 | 107 | 830 | 103 | 79 |
| 6 | 360 | 0.024 | 2.6 | 0.0267 | 107 | 830 | 103 | 77 |

[a] $A = \{[Y(N_2)/Y(O_2)] - 1\}^{-1}$; see Figure 3 and section 3.2.



dx.doi.org/10.1021/jp5020291 | J. Phys. Chem. A 2014, 118, 3237–3242

$Cl + CF_3CF{=}CH_2 \rightarrow CF_3CFClCH_2/CF_3CFCClH_2$.[10] In that study, $k_{Cl}/k_{O2} = 0.0026$ at ambient temperature for the $C_3F_4ClH_2$ radicals formed by Cl addition to the double bond. Uncertainties are discussed in section 3.3.

**3.3. Uncertainty in the Measurements.** All measurements of $k_1$ relative to $k_2$ that were made during these experiments are included in Figure 1. These relative rate ratios have been converted to absolute values of $k_1$ for inclusion in this figure using the temperature-dependent expression for $k_2$ presented above. At ambient temperature, 17 measurements were made, and the 95% confidence limit of these ambient data is ±10%. Each symbol above ambient temperature represents a separate individual measurement of the rate constant ratio again converted to $k_1$. The best estimate of the error in these values is represented by the scatter of the individual points since there is no known systematic error in the measurement of $[C]/[C]_0$ for either $CFCl_2H$ or $CH_4$ in these measurements. Inspecting the data in Figure 1, we estimate the error limits to be ±10% through the entire temperature range studied. This represents the probable error in the rate constant ratios since the rate constant of reaction 2 is assumed to have no error in this calculation. The error in the value of $k_2$ presented above was estimated to be ±11.5%.[1] Combining these estimated errors using the usual expression for ratios, the uncertainty in $k_1$ is calculated to be $[(0.1)^2 + (0.115)^2]^{0.5} = \pm 15\%$ over the entire temperature range.

The uncertainty in the calculation of $k_3/k_4$ at ambient temperature involves two separate issues. First the yield of $CFCl_3$ must be determined in the absence of $O_2$. This is complicated by the entrapment of small amounts of $O_2$ when filling the high-temperature reactor. Because $k_3/k_4$ is very small, a small amount of $O_2$ will depress the $CFCl_3$ yield significantly. For this reason, the best estimate of the $CFCl_3$ yield in $N_2$ is the maximum yield measured during repeat experiments, recognizing that the experimental measurement error in the $CFCl_3$ yield is typically ±10%. At each temperature (see Table 1 for selected examples), the maximum yield was determined to be 100 ± 10%. These measurements in $N_2$ confirm the $CFCl_3$ yield is 100% to within experimental error at ambient temperature and higher temperatures. In the absence of $O_2$, the $CFCl_3$ yield is expected to be 100% as is observed because there is no other plausible consumption path other than reacting with $Cl_2$ in these mixtures. Therefore, we define the $CFCl_3$ yield to be 100% with no error. In the presence of $O_2$, the error in $k_3/k_4$ is governed by the uncertainty in the measured yield of $CFCl_3$; the accuracy of the preparation of the $Cl_2/O_2$ ratio in the mixture; and the amount $O_2$ consumed during the reaction, which is needed to calculate $[O_2]_{av}$. As described above, we have estimated the consumption of $O_2$ and have applied a small correction factor, which changes with the extent of reaction. We believe that the best error limit for $k_3/k_4$ is ±10% indicated by the lines enclosing the data scatter shown in Figure 3 plus an additional 5% for uncertainty in the GC calibration of $CFCl_3$. Thus, the combined error is ±15%.

## 4. CHLORINE CHAIN PROPAGATION IN THE PRESENCE OF $O_2$

In a Fourier-transform infrared spectroscopy (FTIR) study of the Cl-initiated oxidation of $CFCl_2H$ in air at 298 K, Tuazon and Atkinson[5] observed chlorofluoroformaldehyde, C(O)FCl, to be the sole product. This compound was not commercially available for calibration during their study, and the authors could only infer that the yield was 100% because no other products could be seen in the infrared spectrum. They postulated that C(O)FCl is formed from $CFCl_2$ radicals by reactions 4−6 following reaction 1 as discussed above. This mechanism will produce a Cl chain reaction in the presence of $O_2$ analogous to the conventional Cl chain reaction in $N_2$ carried by reaction 3. Therefore, the rate of consumption of $CFCl_2H$ in oxygen should be similar to that in $N_2$ diluent.

In a typical Cl chain abstraction reaction for an alkane such as $C_2H_6$, the consumption of ethane becomes much slower when $O_2$ is added. The $Cl/Cl_2$ chain is terminated by $O_2$ addition to the ethyl radical because it is followed by subsequent reactions of $C_2H_5O_2$, which do not propagate the chain by reforming Cl atoms. This is illustrated in Figure 4A,

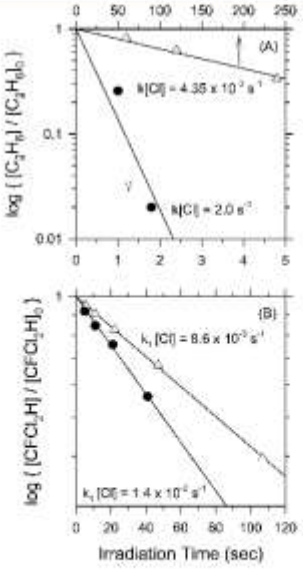


**Figure 4.** (A) Consumption rate of $C_2H_6$ by Cl atoms in $N_2$ (filled circles) and in a $N_2$/20% $O_2$ mixture (triangles) at ambient temperature. (B) Consumption rate of $CFCl_2H$ by Cl atoms in $N_2$ (filled circles) and in a $N_2$/20% $O_2$ mixture (triangles) at ambient temperature.

which is a plot of the $\log_{10}$ of the fractional consumption of $C_2H_6$ versus irradiation time at ambient temperature. The product of the rate constant for the reaction of Cl with $C_2H_6$ ($k_{C2H6} = 5.8 \times 10^{-11}$ cm$^3$ molecule$^{-1}$ s$^{-1}$)[2] times the steady-state Cl atom concentration ($k_{C2H6}[Cl]_{ss}$) can be deduced from the slope of this curve. In $N_2$ diluent, chain propagation leads to a value of $\{k_{C2H6}[Cl]_{ss}\} \approx 2$ s$^{-1}$. Adding 20% $O_2$ to the initial mixture results in a value $\{k_{C2H6}[Cl]_{ss}\} = 0.0044$ s$^{-1}$. Thus, in the presence of 20% $O_2$, the steady-state Cl atom concentration is 450 times smaller, and the rate of $C_2H_6$ consumption slows by the same factor.

Figure 4B shows the results of a similar comparison for reaction 1. In this case, adding 20% $O_2$ to the mixture reduces the consumption rate of $CFCl_2H$ by a factor of only 1.6. This observation shows experimentally that Cl atoms are regenerated efficiently in the presence of $O_2$, as required by reactions 5 and 6 proposed by Tuazon and Atkinson.[5] Thus, in the



dx.doi.org/10.1021/jp5032291 | J. Phys. Chem. A 2014, 118, 3237−3242

presence of $O_2$ the reaction of Cl with $CFCl_2H$ results in a Cl chain reaction consisting of reactions 1 and 4−6. The fact that the chain is propagated by $O_2$ is an interesting and somewhat unusual result.

## 5. SUMMARY

The rate constant of reaction 1 (Cl + $CFCl_2H$) was measured over the temperature range 300−670 K using the relative rate method with $CH_4$ as the reference species. The resulting rate constant expression $k_1 = 1.14 \times 10^{-12} T^{0.49} e^{-241/T}$ $cm^3$ $molecule^{-1}$ $s^{-1}$ (with an error of ±15% including uncertainty in the reference reaction) agrees well with two earlier measurements at lower temperature (298 and 298−435 K).[3,7] Our rate constant measurement provides an extension to a much higher temperature range, offering a well-established reference reaction for relative rate studies, which is a factor of 5 slower than that of methane.

The rate constant ratio for the reaction of $CFCl_2$ with $Cl_2$ relative to that with $O_2$ ($k_3/k_4 = 0.0031 \pm 0.0005$) was measured at ambient temperature. A very slow reaction of another chlorofluorocarbon radical, $CF_3CFCH_2Cl$, with $Cl_2$ relative to $O_2$ has been observed previously.[10]

Finally, experiments in the presence of 20% $O_2$ have shown that a Cl chain reaction occurs in this system that is carried by $O_2$. This occurs because the radical intermediate $CFCl_2O$ formed from $CFCl_2O_2$ can eliminate a Cl atom to form the final product C(O)FCl, thereby regenerating Cl atoms.

## ■ AUTHOR INFORMATION


### Corresponding Author

*(E.W.K.) E-mail: ewkaiser@comcast.net.


### Notes

The authors declare no competing financial interest.

## ■ ACKNOWLEDGMENTS

We thank Professors Craig J. Donahue and Sheila R. Smith for their help during the course of these experiments.

## ■ REFERENCES


(1) Beyukov, M. G.; Slagle, I. R.; Knyazev, V. D. Kinetics of Reactions of Cl Atoms with Methane and Chlorinated Methanes. *J. Phys. Chem. A* **2002**, *106*, 10532−10542.

(2) Beyukov, M. G.; Slagle, I. R.; Knyazev, V. D. Kinetics of Reactions of Cl Atoms with Ethane, Chloroethane, and 1,1-Dichloroethane. *J. Phys. Chem. A* **2003**, *107*, 6565−6573.

(3) Talhaoui, A.; Louis, F.; Meriaux, B.; Devolder, P.; Sawerysyn, J.-P. Temperature Dependence of Rate Coefficients for the Reactions of Chlorine Atoms with Halomethanes of Type $CHCl_{3-x}F_x$ ($x = 0$, 1, and 2). *J. Phys. Chem.* **1996**, *100*, 2107−2113.

(4) Louis, F.; Talhaoui, A.; Louis, F.; Sawerysyn, J.-P.; Rayez, M.-T.; Rayez, J.-C. Rate Coefficients for the Gas Phase Reactions of $CF_3CH_2F$ (HFC-134a) with Chlorine and Fluorine Atoms: Experimental and ab Initio Theoretical Studies. *J. Phys. Chem. A* **1997**, *101*, 8503−8507.

(5) Tuazon, E. C.; Atkinson, R. Tropospheric Transformation Products of a Series of Hydrofluorocarbons and Hydrochlorofluorocarbons. *J. Atmos. Chem.* **1993**, *17*, 179−199.

(6) Kaiser, E. W.; Wallington, T. J.; Hurley, M. D. Products and Mechanism of the Reaction of Cl with Butanone in $N_2/O_2$ Diluent at 297−526 K. *J. Phys. Chem. A* **2009**, *113*, 2424−2437.

(7) Tuazon, E. C.; Atkinson, R.; Corchnoy, S. B. Rate Constants for the Gas-Phase Reactions of Cl Atoms with a Series of Hydrofluorocarbons and Hydrochlorofluorocarbons at 298 K. *Int. J. Chem. Kinet.* **1992**, *24*, 639−648.

(8) Glavas, S.; Heicklen, J. Relative Reactivity of Chlorine Atoms with NO, $NO_2$, and $HCCl_2F$ at Room Temperature and Atmospheric Pressure. *J. Photochem.* **1985**, *31*, 21−28.

(9) Jourdain, J. L.; Poulet, G.; Barrasin, J.; LeBras, G.; Combourieu, J. Mecanismes chimiques de la pollution atmospherique par les composes halogenes: etude cinetique de reactions elementaires possibles. *Pollut. Atmos.* **1977**, *75*, 256−259.

(10) Kaiser, E. W.; Wallington, T. J. Relative Rate Study of the Kinetics, Mechanism, and Thermodynamics of the Reaction of Chlorine Atoms with $CF_3CF{=}CH_2$ (HFO-1234yf) in 650−950 Torr of $N_2$ or $N_2/O_2$ Diluent at 296−462 K. *J. Phys. Chem. A* **2012**, *116*, 5958−5971.